CENTRO DE INVESTIGACIONES
EN OPTICA, A.C.

“SYNTHESIS AND CHARACTERIZATION OF PHOTOTHERMAL CERAMIC PARTICLES FOR USE IN PRINTED ANTI-COUNTERFEITING APPLICATIONS”

Tesis que para obtener el grado de Doctor en Ciencias (Óptica)

Presenta: Jorge Alberto Molina González

Director de Tesis: Dr. Haggeo Desirena Enrriquez

León · Guanajuato · México
Enero de 2022

Versión definitiva.
Incluye cambios sugeridos por revisores

Vo. Bo.
Dr. Haggeo Desirena Enrriquez
16 de enero 2022

PhD Thesis:

Synthesis and characterization of photothermal ceramic particles for use in printed anti-counterfeiting applications

As a prerequisite for obtaining the degree of:

PhD in Science (Optics)

Submit:

MSc. Jorge Alberto Molina González

Advisor:

Dr. Haggeo Desirena Enrriquez

A las almas que son eternidad,
Gerardito, Tano va por ustedes.

Agradecimientos

Han pasado ya seis años desde la primera vez que me tocó plasmar en unas páginas el conocimiento adquirido después de una etapa en el laboratorio. Y a pesar de que en este momento lo haré por tercera vez, sigue siendo necesario dar reconocimiento a personas clave que compartieron tiempo en dicho proceso. Por lo anterior, en los siguientes párrafos trataré de plasmar mi agradecimiento a cada una de ellas, sin olvidar a cada una de las personas que se cruzaron en mi camino para aportarme algo, aunque sólo haya sido un periodo determinado, gracias. Si olvido nombrar a alguno no lo tomen a mal, aunque cada uno sabe lo que influyó en mí y eso lo agradezco.

En primer lugar, como siempre ha sido, agradezco de manera infinita a mis padres. Ustedes sentaron la base de lo que soy, y este logro sólo es posible gracias a ustedes. Mamá, el ser humano que soy es producto de tus manos, ya que desde mi primer respiro has influido en demasía en mi formación y en este punto te digo que los aplausos son para ti. Noé y Brenda, hermanos míos, han sido cuna y soporte de mi travesía en la ciencia, ustedes han estado para mí desde que los conocí, gracias por soportar cada una de las cosas que me implican, en especial las bromas y ausencias. A mi familia, a pesar de mis desapariciones siguen recibiéndome y aplaudiendo cada paso que doy.

Agradezco a cada una de mis amistades, Dora, Andrea, Bobby, Diego, Itzel,

Priscilla, Gonzalo, Lety. Por los años han seguido conservando la amistad y contacto, lo cual les agradezco enormemente. Han sido apoyo y escucha de todos mis momentos, los excitantes y aquellos más pesados, en cada uno de ellos estuvieron presentes. Agradezco a las personas que han llegado y sorpresivamente me han brindado su amistad. "Los Pablitos", gracias por cada una de las tardes de platica, en especial a Andrés y Mariana, gracias por escuchar abiertamente. No puedo olvidar los viajes más recientes acompañados de personas como Simón y Areli, gracias por mostrarme una visión más relajada de la vida. Mar, no imaginaría que desde hace muchos años estaba a una persona de conocerte, llegaste a romper y a crear, llegaste con un corazón abierto y sólo puedo decir gracias, gracias por cada segundo que decides estar conmigo, todo ese amor y ese apoyo los siento y te digo: esto es sólo el comienzo.

Quiero agradecer a Milvia y José, personas con las que pude desarrollar una amistad totalmente profunda en el CIO, sin embargo, sé que será para toda la vida. Gracias por cada momento, plática, brindis y demás experiencias vividas, sin ustedes el CIO no hubiera sido tan divertido. A cada una de las personas que estuvieron en la oficina 1351, en especial a Cruz, Arturo y Chayito, sé que les espera lo mejor por su profesionalismo, gracias por su amistad. Agradezco a cada persona que me cruce en los pasillos y permitió poder desarrollar mi proyecto y persona. Doy gracias a cada miembro de la mesa de los capítulos estudiantiles, me permitieron desarrollar habilidades que no sabía que tenía. Sé que todos los que formamos parte lo hacemos con una intensión totalmente noble, la divulgación. Sé que queda en buenas manos y me entusiasma saber todo lo que lograran.

Sin dudarlo, sé que cada uno de los miembros del CIO hacen lo que está en sus manos para poder encaminarlo hacía un futuro mejor. Sin embargo, quiero agradecer de manera especial a Christian Albor por cada una de las actividades en las que me

ayudaste, aconsejaste y escuchaste, te conocí como técnico y te convertiste en mi amiga. Ricardo Valdivia, eres ya una leyenda en el CIO, gracias por tu apoyo y cada una de las recomendaciones de música que me hiciste. Agradezco a Narahí, Marlen e Itzel por su ayuda y trabajo, sin dudarlo los estudiantes estaríamos perdidos sin ustedes. Lucy y Chayito, gracias por las bromas y atenciones brindadas en todos los momentos que las vi. Gaby y Angeles, agradezco enormemente su dedicación en la biblioteca y en la organización de fiestas que propician una convivencia más amena entre estudiantes. Agradezco a los profesores que me impartieron cada uno de los cursos, Enrique Castro, Mario Ruiz, Joel Briones, Alfonso Vázquez, gracias.

Agradezco cada una de las observaciones del comité de seguimiento, doctores Luis Armando Diaz, Enrique Castro y Marco Antonio Meneses, muchos de sus comentarios perfilaron el trabajo hacia una calidad mayor. Agradezco a los sinodales, Dr. Alfredo Benitez, Dra. Tzara López, Dr. Gonzalo Ramirez, por el tiempo y comentarios hacia este trabajo, sin duda puedo decir que me permitieron formar una tesis de la que estoy orgulloso. De igual manera agradezco al Dr. Octavio Meza por su aportación en el modelo teórico desarrollado en la presente tesis.

Dr. Haggeo Desirena, desde la primera clase que tomé con usted, me mostró una pasión y emoción por la ciencia que pocos tienen. Fueron siete años de trabajo en los cuales aprendí y desarrollé habilidades en mí, gracias. La confianza y libertad de trabajo que me entregó me permitieron desarrollar un juicio del cual estoy orgulloso. Recordaré de manera muy especial todas las horas de discusión que tuvimos, agradezco que siempre me viera como un igual y mi opinión la valorara como un profesional. Le agradezco los consejos profesionales y personales, en gran medida influyeron en los resultados que hemos obtenido. Agradezco a cada miembro del grupo de investigación, los cuales son muchos, pero en especial a Abril, Ignacio, Priscilla y Fer, sin duda los momentos en el laboratorio fueron más amenos con ust-

edes. Agradezco a cada miembro de la sociedad que noblemente hace lo que está en sus manos por un país y mundo mejor.

Agradezco a CONACYT por la beca otorgada durante mis estudios de posgrado. El apoyo 288572 fue indispensable para la compra de equipo y consumibles fundamentales para la conclusión de mi trabajo.

Gracias a la vida.

Abbreviations

The following list shows the abbreviations used in the text

Ln^{3+}	Trivalent lanthanide
RE^{3+}	Trivalent rare earth
LD	Laser diode
xrd, XRD	X-ray diffraction
sem, SEM	Scanning Electron Microscopy
PTT	Photothermal
NIR	Near-infrared spectrum

Abstract

Due to the constant evolution of counterfeiting media, it is necessary to improve anti-counterfeiting technology. Hence, the main objective of this research work was the design of security systems based on the PTT effect of materials. For this purpose, Ln^{3+} doped ceramic particles, whose PTT response was optimized, were fabricated in order to be used in real printed applications.

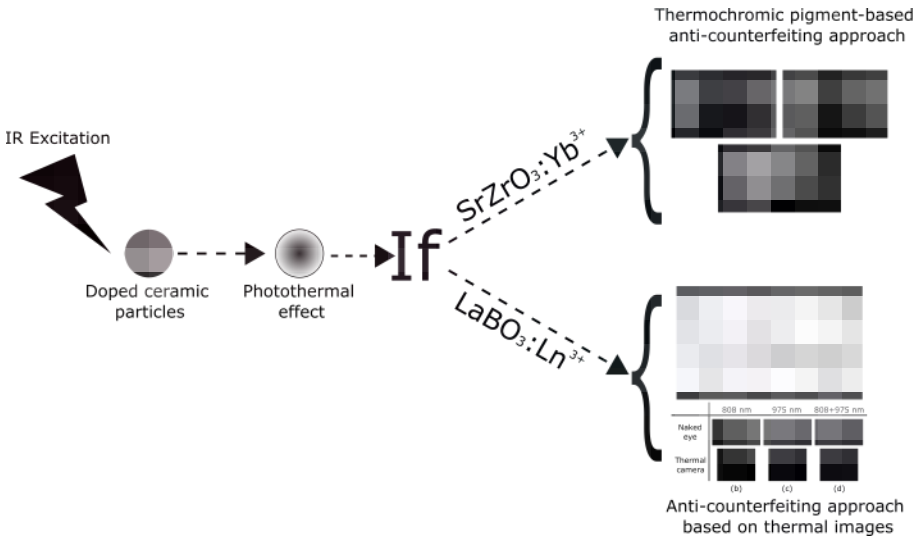

In the first approach, Sr/Zr ceramic oxides doped with Yb^{3+} were synthesized. A photothermal ink was prepared with the Sr/Zr particles. In conjunction with the thermochromatic ink, based on a reversible thermochromatic pigment, a printed security system was designed, fabricated and tested. This was evaluated with mul-

tiple NIR wavelengths and under external heat sources and it was determined that only by exciting with the absorption wavelength of the oxides was the photothermal effect generated, which produced the heating of the thermochromatic ink and thus the information was revealed.

For the second approach, $LaBO_3 : Nd^{3+}$ and $LaBO_3 : Yb^{3+}$ particles were fabricated separately, whose photothermal response is more efficient than that of $Sr/Zr : Yb^{3+}$. This effect is selective, i.e. they only responded to a specific and different NIR wavelength from each other. With these, multilayer printed codes were designed, which were only revealed using a thermal camera when excited by the specific wavelengths for each layer. The verification of the code is given with a sequence determined by the order of the layers. To improve the level of security, commercial particles with frequency upconversion were added, so that the verification of the information was performed through both the thermal and the visible imaging channel.

The proposed strategies show potential to be applied in different items, shown as examples medicine packaging, business cards, etc. Moreover, within the scientific character, the synthesized samples show a more efficient photothermal response when compared to lanthanide-doped materials reported in the literature.

Resumen

Debido a la constante evolución de los medios de falsificación, es necesario mejorar la tecnología antifalsificación. Por ello, el objetivo principal de este trabajo de investigación fue el diseño de sistemas de seguridad basados en el efecto PTT de los materiales. Para ello, se fabricaron partículas cerámicas dopadas con Ln^{3+}, cuya respuesta PTT fue optimizada, con el fin de ser utilizadas en aplicaciones impresas reales.

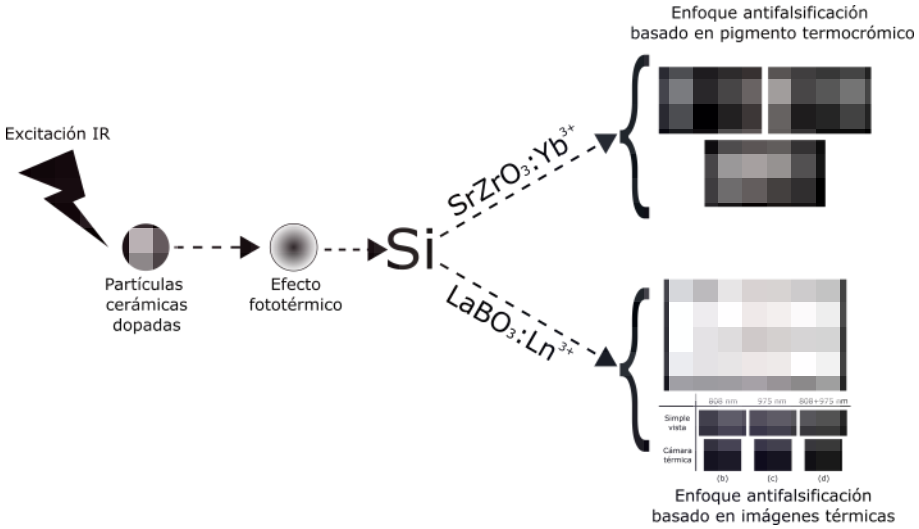

En la primera aproximación se sinterizaron partículas de óxidos cerámicos de Sr/Zr dopados con Yb^{3+} para preparar una tinta fototérmica. En conjunto con la tinta termocromática, basada en un pigmento termocromatico reversible, se diseñó,

fabricó y probó un sistema de seguridad impreso. Este fue evaluado con múltiples longitudes de onda de la región NIR y bajo fuentes de calor externas y se determinó que sólo excitando con la longitud de onda de absorción de los óxidos era generado el efecto fototérmico, el cual producía el calentamiento de la tinta termocromatica y por ende la información era revelada.

Para la segunda aproximación, se fabricaron partículas de $LaBO_3 : Nd^{3+}$ y $LaBO_3 : Yb^{3+}$ de manera separada, cuya respuesta fototérmica es más eficiente que la de $Sr/Zr : Yb^{3+}$. Dicho efecto es selectivo, es decir sólo respondían a una longitud de onda especifica NIR y diferente entre ellas. Con estas, se diseñaron códigos impresos multicapa, los cuales fueron revelados únicamente utilizando una cámara térmica al ser excitados por las longitudes de onda específicas para cada capa. La verificación del código se da con una secuencia determinada por el orden de las capas. Para mejorar el nivel de seguridad, se añadieron partículas comerciales con conversión ascendente de frecuencia, así la verificación de la información se realizaba a través del canal de imagen térmico y el visible.

Las estrategias propuestas muestran potencial para ser aplicados en distintos artículos, mostrados como ejemplos empaques de medicamentos, tarjetas de presentación, etc. Además, dentro del carácter científico, las muestras sintetizadas muestran una respuesta fototérmica más eficiente si se comparan con materiales dopados con lantánidos reportados en la literatura.

Contents

Chapter 1

Introduction

Counterfeiting is a serious global problem causing damage in multiple sectors [1]. According to the World Trade Organization (WTO), counterfeiting can be defined as the *"Unauthorized representation of a registered trademark on goods identical or similar to the goods for which the trademark is registered, in order to deceive the purchaser into believing that he is buying the original goods"* [2]. On the other hand, according to the International Anti-Counterfeiting Coalition (IACC), counterfeiting is *"an article that uses another's trademark without their permission"* [3]. Therefore, in simplified terms, counterfeiting is a crime that encompasses the unauthorized manufacture, distribution, or marketing of products.

At first glance, the direct damages appear to be those suffered by consumers, legitimate manufacturers, and brand owners. However, the social and economic impact is global in scale and causes damage even to the state. Although the information on counterfeiting is often scattered, the Business Action to Stop Counterfeiting and Piracy (BASCAP) of the International Chamber of Commerce (ICC) has compiled information and a series of predictions on the impact of counterfeiting [1]. According to it, in 2013 the value produced in international trade by counterfeit products

was approximately USD 923 billion, although it could escalate to USD 1.13 trillion if digital trade is considered. With the growth of counterfeiting over the years, by 2022 the value of economic losses could reach an unimaginable USD 2.81 trillion. In addition to economic losses, the licit manufacturers or brand owners of different sectors as apparel and footwear, electronics, books, automotive, among others are exposed to a loss of credibility associated with the lack of quality of illicit products [4].

Consumers are not only exposed to low-quality products, but their health is also at risk when consuming products of dubious origin such as food or medicines. The latter may not comply with the correct formulation, may have been extracted before labeling, and therefore may not comply with proper storage conditions [4]. In fact, the pharmaceutical industry is one of the fields with the greatest negative impact due to products of illicit origin, which could contribute to the detriment of the health of consumers [5, 6]. According to the National Association of Boards of Pharmacy, profits from fraudulent drugs reach up to 75 billion dollars annually, which is even higher than the income from legitimate means [4]. The World Health Organization (WHO) estimates that 10 percent of the available drug market in some developing countries is counterfeited [4, 7–9]. Although in developed countries the figure drops to 1 percent, it is difficult to calculate the number of deaths caused by fraudulent drugs. Interpol estimates that there are around one million a year, just to give an idea of the magnitude [10].

The damage produced by counterfeit products not only has an economic impact but there is also a very clear social damage [4,11]. When a product is sold outside the law, such transaction does not generate any tax payment, which directly affects the funds of state, limiting the financial resource for the operation of government [12]. Not only business products can be counterfeited, but also certain official documents, such as passports, licenses, or identification cards, which are often used for crimes

such as extortion or fraud or even high-level crimes such as terrorism [13].

In order to focus attention on illegal trade and/or counterfeiting of physical products or official documents, there are several mechanisms for their protection. These must be simple to decipher for consumers, semi-confidential for distributors or sellers, and strictly secret for manufacturers, considering that each of them corresponds to a link in a supply chain [4]. Ideally, an anti-counterfeiting system should be non-cloneable, easy to implement, difficult to remove-reuse, and easy to decode (simple equipment). On the other hand, according to the Food and Drugs Administration (FDA), the technology should not be restrictive, i.e., it should be versatile so that it can be implemented in different products by varying the shape and/or substrate [5].

Commercially there are several security technologies, such as holograms, bar codes, quick response codes, radio frequency identification, among others [5]. Although each of these technologies offers advantages, they still do not meet all of the above criteria for an ideal printed security system [14]. For this reason, and given the growth of counterfeit technology, the private and public sectors are constantly evolving to design more secure systems that are adaptable to current requirements. Thus, several research groups have decided to contribute their knowledge to prevent counterfeiting. In general, the proposals usually include the development of a material that is used to print a hidden code that can only be decoded by receiving a specific stimulus.

In recent years, the spectroscopic properties of luminescent materials have been explored for encoding information for use in printed security applications. Due to the great variety of materials in the literature, especially those doped with Ln^{3+}, there are several approaches used in anti-counterfeiting applications, such as single and multiple emissions, tunable decay time, orthogonal upconversion emission, thermal properties, or more complex ones such as the combination of upconversion with

plasmonic properties [14–20]. All of the above configurations respond when excited with light at specific wavelengths, however, the decoding of the hidden information can be simple by involving sight alone or increasing in complexity using highly specialized equipment [21]. Similarly, decoding can be done in steady-state or dynamic, depending on the excitation waveform [21, 22]. The resolution process can become more complex if it is made dependent on external stimuli, such as temperature [23]. However, normally, increasing the complexity of resolution also increases the cost of manufacturing the security system, as well as the cost of the equipment used for it. For this reason, despite the advantages offered by the above mechanisms, there are still characteristics that limit their practical application, such as the cost and time of the synthesis of the base materials, as well as the equipment necessary for their manufacture and those used for decoding [14, 19–21].

Printed security systems need to be constantly evolving, increasing the complexity of being counterfeited, but trying to maintain accessibility. This is why it is necessary to explore new ways of encoding information, such as including new mechanisms to hide information. For example, few works use temperature as a variable in the security process, either as an external stimulus or generated directly in the material. Dong et al. designed nanoparticles with upconversion emission, $NaYF_4 : Yb^{3+}/Ln^{3+}$ and $NaGdF_4 : Yb^{3+}/Ln^{3+}$ (Ln= Ho, Tm), which present different negative thermal quenching, so when using temperature the color coordinate of the print varied [23]. Similarly, Lei and coworkers designed a security system based on Na_3ZrF_7 nanoparticles, which increased the emission intensity of the print when heated [24]. Although both approaches show a new alternative in Ln^{3+}-based security systems, they have some drawbacks such as the long synthesis of the materials or the need for an external heat source or a variable power laser for decoding. Similarly, few studies use the temperature generated by the materials when irradiated with light (PTT) to hide

information. Another interesting work is the one published by Kang et al, in which gold nanoparticles of different sizes are used to hide information in printed form [25]. By having different sizes, the metal nanoparticles have a different resonance plasmon, therefore when irradiated at these wavelengths the temperature of the print increases and can be observed only through a thermal camera. However, a drawback is the large absorption bandwidths, which can affect the multiple wavelengths that reveal the thermal image. This can be solved by designing materials with sharp and discrete absorption bands, such as those doped with Ln^{3+}. Although not used for security, Wang and co-workers showed that a Ln^{3+}-doped matrix can generate a PTT effect. They synthesized $NaYF_4 : 25Er^{3+}$ microparticles, which upon irradiation with a 1550 nm LD at 2.05 W/cm^2 raised their temperature up to 49.3 °C [26].

In the present work, two approaches to security systems based on Ln^{3+}-doped materials are studied. The first approach was developed using synthesized and optimized Yb^{3+} doped Sr/Zr microparticles, since low thermal conductivities, extraordinary thermal stabilities, and high solubility of Ln^{3+} ions have been reported for these materials [27]. It is worth mentioning that, to our knowledge, these materials have not been used in anti-counterfeiting applications. Structural characterization and spectroscopy of the synthesized materials were performed, as well as PTT characterization using NIR LD radiation as excitation. A rate equation model was designed to explain the thermal conversion efficiency. Combined with a thermochromatic pigment, for the first time, two types of security systems were designed, fabricated, and tested, which require only a fixed power LD for decoding, which is based on the color change of the pigment caused by the heating of Sr/Zr PTT particles. On the other hand, in the second proposal, $LaBO_3 : Ln3+$ (Ln=Nd^{3+}, Yb^{3+}) microparticles were used as a base, since they have high thermal stability, exceptional optical damage threshold, and low thermal conductivity. Once the structural, spectroscopic, and

PTT characterization was performed, a security system based on thermal imaging was designed. The synthesized particles were combined with a varnish to print codes by screen printing. These, when irradiated with the appropriate wavelength, increase their temperature which generates thermal images that are only visible through a thermal camera. As a proof of concept, it was printed on different substrates, demonstrating the versatility of the designed system.

Bibliography

[1] BASCAP-INTA. The economic impacts of counterfeiting and piracy. https://iccwbo.org/publication/economic-impacts-counterfeiting-piracy-report-prepared-bascap-inta/, 2016.

[2] World Trade Organization. GLOSSARY TERM. https://www.wto.org/english/thewto_e/glossary_e/counterfeit_e.htm, 2020.

[3] International AntiCounterfeiting Coalition. About Counterfeiting. https://www.iacc.org/resources/about/what-is-counterfeiting, 2020.

[4] Klara Dégardin, Yves Roggo, and Pierre Margot. Understanding and fighting the medicine counterfeit market. *Journal of Pharmaceutical and Biomedical Analysis*, 87:167–175, 2014. Review Papers on Pharmaceutical and Biomedical Analysis 2013.

[5] Dipika Bansal, Swathi Malla, Kapil Gudala, and Pramil Tiwari. Anti-counterfeit technologies: A pharmaceutical industry perspective. *Scientia Pharmaceutica*, 81(1):1–14, 2013.

[6] Erwin A. Blackstone, Joseph P. Fuhr, , and Steve Pociask. The health and economic effects of counterfeit drugs. *American Health & Drug Benefits*, 7:216–224, 2014.

[7] Heyang Zhang, Dawei Hua, Chaobo Huang, Sangram Keshari Samal, Ranhua Xiong, Félix Sauvage, Kevin Braeckmans, Katrien Remaut, and Stefaan C. De Smedt. Materials and technologies to combat counterfeiting of pharmaceuticals: Current and future problem tackling. *Advanced Materials*, 32(11):1905486, 2020.

[8] Theodoros Kelesidis and Matthew E. Falagas. Substandard/counterfeit antimicrobial drugs. *Clinical Microbiology Reviews*, 28(2):443–464, 2015.

[9] World Health Organization. 1 in 10 medical products in developing countries is substandard or falsified. https://www.who.int/news/item/28-11-2017-1-in-10-medical-products-in-developing-countries-is-substandard-or-falsified, 2017.

[10] Natalie Southwick. Counterfeit Drugs Kill 1 Mn People Annually: Interpol. https://insightcrime.org/news/brief/counterfeit-drugs-kill-1-million-annually-interpol/, 2013.

[11] Bora Yoon, Jung Lee, In Sung Park, Seongho Jeon, Joosub Lee, and Jong-Man Kim. Recent functional material based approaches to prevent and detect counterfeiting. *J. Mater. Chem. C*, 1:2388–2403, 2013.

[12] John Spink, Douglas C. Moyer, Hyeonho Park, and Justin A. Heinonen. Defining the types of counterfeiters, counterfeiting, and offender organizations. *Crime Science*, 2:1–10, 2013.

[13] Rafael Vieira, Catarina Silva, Mário Antunes, and Ana Assis. Information system for automation of counterfeited documents images correlation. *Procedia Computer Science*, 100:421–428, 2016.

[14] Kisun Park, Minji Park, Ho Seong Jang, Ji Hun Park, Jaekyun Kim, Younghak Cho, Il Ki Han, Dongjin Byun, and Hyungduk Ko. Highly secure plasmonic encryption keys combined with upconversion luminescence nanocrystals. *Advanced Functional Materials*, 28(21):1800369, 2018.

[15] Ziyong Cheng and Jun Lin. Synthesis and application of nanohybrids based on upconverting nanoparticles and polymers. *Macromolecular rapid communications*, 36(9):790–827, 2015.

[16] Wei Ren, Gungun Lin, Christian Clarke, Jiajia Zhou, and Dayong Jin. Optical nanomaterials and enabling technologies for high-security-level anticounterfeiting. *Advanced Materials*, 32(18):1901430, 2020.

[17] Xiaoqian Ge, Jinliang Liu, and Lining Sun. Controlled optical characteristics of lanthanide doped upconversion nanoparticles for emerging applications. *Dalton Transactions*, 46(48):16729–16737, 2017.

[18] Cecile Chenot, Raphael Robiette, and Sonia Collin. First evidence of the cysteine and glutathione conjugates of 3-sulfanylpentan-1-ol in hop (humulus lupulus l.). *Journal of agricultural and food chemistry*, 67(14):4002–4010, 2019.

[19] Tianying Sun, Bingzhe Xu, Bing Chen, Xian Chen, Mingyu Li, Peng Shi, and Feng Wang. Anti-counterfeiting patterns encrypted with multi-mode luminescent nanotaggants. *Nanoscale*, 9(8):2701–2705, 2017.

[20] Minli You, Min Lin, Shurui Wang, Xuemin Wang, Ge Zhang, Yuan Hong, Yuqing Dong, Guorui Jin, and Feng Xu. Three-dimensional quick response code based on inkjet printing of upconversion fluorescent nanoparticles for drug anti-counterfeiting. *Nanoscale*, 8(19):10096–10104, 2016.

[21] Yiqing Lu, Jiangbo Zhao, Run Zhang, Yujia Liu, Deming Liu, Ewa M Goldys, Xusan Yang, Peng Xi, Anwar Sunna, Jie Lu, et al. Tunable lifetime multiplexing using luminescent nanocrystals. *Nature Photonics*, 8(1):32–36, 2014.

[22] Yangyang Du, Yunfeng Wang, Zhiqin Deng, Xian Chen, Xueqing Yang, Tianying Sun, Xin Zhang, Guangyu Zhu, Siu Fung Yu, and Feng Wang. Blue-pumped deep ultraviolet lasing from lanthanide-doped lu6o5f8 upconversion nanocrystals. *Advanced Optical Materials*, 8(2):1900968, 2020.

[23] Yanqing Hu, Qiyue Shao, Xinyi Deng, Dongdong Song, Shouyu Han, Yan Dong, and Jianqing Jiang. Thermally induced multicolor emissions of upconversion hybrids with large color shifts for anticounterfeiting applications. *Journal of Materials Chemistry C*, 7(38):11770–11775, 2019.

[24] Lei Lei, Daqin Chen, Can Li, Feng Huang, Junjie Zhang, and Shiqing Xu. Inverse thermal quenching effect in lanthanide-doped upconversion nanocrystals for anti-counterfeiting. *Journal of Materials Chemistry C*, 6(20):5427–5433, 2018.

[25] Hongki Kang, Jee Woong Lee, and Yoonkey Nam. Inkjet-printed multiwavelength thermoplasmonic images for anticounterfeiting applications. *ACS applied materials & interfaces*, 10(7):6764–6771, 2018.

[26] Hong Wang, Xiumei Yin, Mingming Xing, Yao Fu, Ying Tian, Xin , Tao Jiang, and Xixian Luo. Investigation on the thermal effects of nayf 4: Er under 1550 nm irradiation. *Physical Chemistry Chemical Physics*, 19(12):8465–8470, 2017.

[27] Jorge Molina-González, Abril Arellano-Morales, Octavio Meza, Gonzalo Ramírez-García, and Haggeo Desirena. An anti-counterfeiting strategy based

on thermochromic pigment activated by highly yb3+ doped photothermal particles. *Journal of Alloys and Compounds*, 850:156709, 2021.

Chapter 2

Photothermal effect on crystalline ceramic materials

2.1 Ceramics

A crystal has a three-dimensional and large molecular periodic arrangement. Fig. (2.1) illustrates the difference between the crystalline and amorphous arrangement of SiO_2.

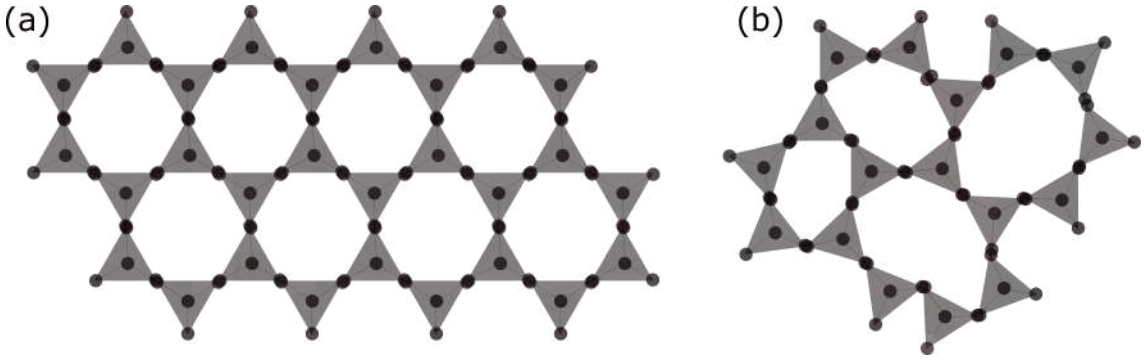

Figure 2.1: Atomic arrangement (a) crystalline and (b) amorphous for SiO_2.

The way to characterize a crystal is by means of the atomic arrangement in which the elements of the material are found. There are seven crystalline systems described by geometry, known as cubic, tetragonal, orthorhombic, rhombohedral (trigonal), hexagonal, monoclinic, and triclinic (fig. (2.2) [1].

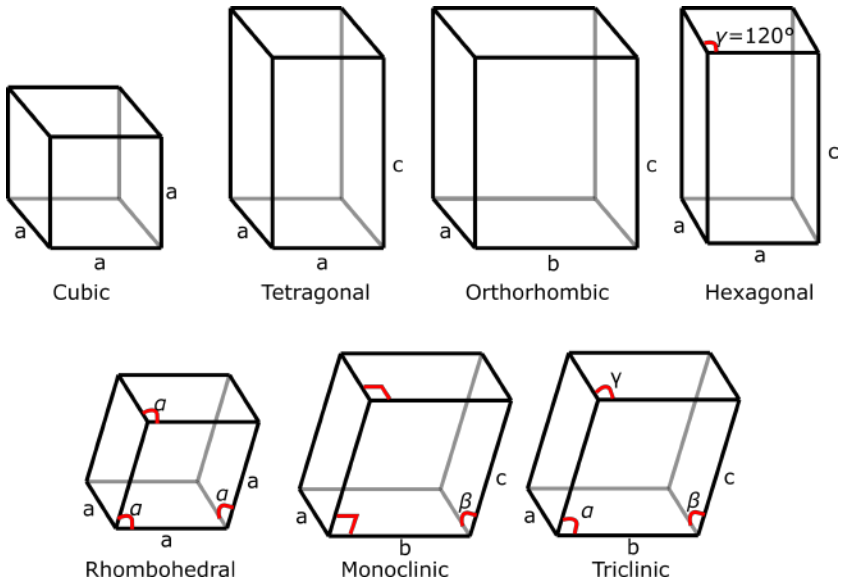

Figure 2.2: Seven crystalline systems.

The values indicated by a, b, c, and α, β, γ are known as network parameters. They indicate the axial lengths or dimensions of the unit cell (a, b, c) and the interaxial angles (α, β, γ).

The formation of a crystalline composite solid structure can occur by means of a solid solution, which occurs by reacting two solid compounds. For the occurrence of a solid solution the following points must be considered:

- *Size*: the difference between the ionic radii of the two compounds should be small, i.e., a difference of less than 15 % should be present in order to avoid lattice deformations.

- *Crystalline structure*: Preferably the materials should have the same crystalline structure since otherwise the generation of spurious phases could occur.

- *Valence*: The ions must have the same valence in order to be able to be dissolved in each other. The difference between valences promotes the generation of compounds instead of solutions.

- *Electronegativity*: The atoms must have a similar electronegativity, otherwise the generation of a compound instead of a solution is promoted.

Ceramics are inorganic materials made up of metallic and non-metallic compounds, whose predominant bonds can be ionic or covalent. The atomic arrangement shows a long-range order, which extends to scales much larger than 10 nm. In general, a ceramic, unlike a single crystal, is a polycrystalline material, which indicates that it is composed of smaller crystals, usually oriented in different spatial directions. These smaller components are called grains. The order type in crystalline materials can be detected by xrd [1, 2].

There are several classifications that can be given to ceramics, such as their composition (oxides, carbides, nitrites, sulfides, fluorides, etc.) or their application (electrical, magnetic, optical, automotive, mechanical, biomedical, construction, chemical, etc.) [1–3]. Due to the diversity of ceramic materials, it is complicated to make a general definition of them. However, according to W.D. Kingery the most general way to define them is "A non-metallic inorganic solid" [2].

The properties conferred by the types of bonds that make up ceramic materials generally include high melting points, structural rigidity, thermal insulation, and brittleness [2, 4, 5]. Due to the nature of the material itself, high sintering temperatures are required for its synthesis, which normally starts with powders (precursors).

2.2 Low thermal conductivity host oxides

Zirconium oxide has been widely used due to its properties that make it a material with multiple technological applications. Mainly, its mechanical properties (high hardness), high melting point, mainly determined by the covalent bond in its structure, stand out. Optically, it has a high refractive index, transparency in the visible region of the electromagnetic spectrum, and an outstanding threshold to optical damage. Among its thermal properties are its low thermal conductivity and its chemical and physical stability at elevated temperatures, which have been exploited in thermal barrier applications. Among other applications is its use in catalysts, sensors, dielectric devices, ceramic materials for biological applications.

Due to its crystalline structure, properties can vary within a material. Zirconium oxide has three phases that can be modified according to temperature, which are monoclinic (room temperature), tetragonal (1170 °C), and cubic (2370 °C). However, stabilization of the tetragonal and cubic phases can be achieved at lower temperatures if dopant oxides, such as Y^{3+} or Yb^{3+} oxides, are added. This ion doping generates a number of charge "compensator" called vacancies, thus preserving electrical neutrality. By significantly increasing the bend concentration, it is possible to generate an element known as rare earth zirconate $M_2Zr_2O_7$ (where M is a rare earth element). Such materials exhibit improved thermal insulation and durability when compared to the cubic phase ZrO_2. Crystallized in pyrochlore structure or in fluorite structure, rare earth zirconates have a high content of structural oxygen vacancies, resulting in strong phonon dispersion and a significant reduction in thermal conductivity.

Strontium zirconate belongs to the family of alkaline earth zirconate oxides with perovskite-like structure. Alkaline earth zirconate hosts are known for their out-

standing properties, such as high thermal and chemical stability, single-phase crystal structure, high refractive index and wide band gap, so they have potential in the electronic ceramics industry, gas sensors, optical coatings and filters, among others. Due to their thermal stability properties, they are used as a special class of crucibles for the synthesis of superconductors, refractory materials and deposition substrates. Compared to other materials with low thermal conductivities such as c-ZrO_2 or $M_2Zr_2O_7$, alkaline earth zirconates, especially $SrZrO_3$, have the advantage of being synthesized at lower temperatures, their thermal conductivity is low and the reagents needed for their preparation are cheaper. For these reasons, $SrZrO_3$ turns out to be a good alternative to be a material used in thermal barrier coatings. On the other hand, its ability to be a host for lanthanide ions has been explored, with which interesting luminescent properties have been obtained.

Rare earth borates have been under study since the 1960s. $LaBO_3$ and $NdBO_3$ are isomorphous with the structure of aragonite, while by reducing the size of the ion at the rare earth position, the structure of calcite can be obtained. The main interest of these systems is focused on their possible uses as recovery materials in nuclear reactor devices, as well as in technological fields; due to their thermal stability, the ability to be present in glass formation and their luminescent properties. For example, europium-doped $(Gd, Y)BO_3$ is an interesting system for display panels with high photoluminescence (PL) emission properties that are strongly affected by particle morphology and size, and relative lanthanide concentrations. In addition, YBO_3-doped lanthanide ions possess high photoluminescence efficiency under VUV excitation and good dielectric properties. Therefore, this nanoscale-reduced material has attracted great attention for its potential applications in miniaturized devices. Due to their UV transparency and extraordinary optical damage threshold, rare earth borates are superior to other nonlinear materials in applications involving

UV excitation. Although little explored, having an orthorhombic structure, $LaBO_3$ and $NdBO_3$ have low thermal conductivities of less than 6 W/mK, which can be exploited in applications where poor heat dissipation is required.

2.3 Thermal conductivity

In general, heat transfer between two systems is nothing more than the transfer of internal energy. This happens by means of three processes, conduction, convection, and radiation. In practice, in many cases, there is usually a combination of these [6,7].

Heat conduction is the process of energy exchange from one body to another, or from one part of a body to another through the exchange of kinetic energy from the movement of molecules by direct communication. The flow of energy goes from molecules of higher energies to those with a lower amount (higher at a lower temperature). Characteristically, this process occurs within the physical limits of the body or through two bodies in contact.

Heat conduction can be described in terms of fig. (2.3). Considering a plate of surface A with thickness Δx. The two faces are at a temperature difference $t_1 - t_2$, where $t_1 > t_2$. Because of this, there is a heat flow whose velocity is q (energy per unit time), which is described by eq. (2.1).

$$q = kA\frac{t_1 - t_2}{\Delta x} \tag{2.1}$$

From eq. (2.1), the proportionality constant k is the thermal conductivity of the material of which the plate is made, whose units in the international system are W/mK. It is an intrinsic property of the material and depends only on its chemical composition and not on its geometrical configuration [8].

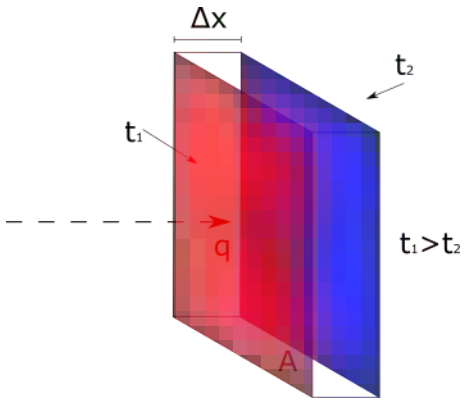

Figure 2.3: Descriptive diagram of the heat conduction process. It is a plate of area A, temperatures t_1 and t_2, a thickness Δx and q the heat flow velocity.

Considering that heat conduction is nothing more than the transmission of energy due to molecular motion, thermal conductivity is the physical property that indicates how easily such transmission can take place in a material. It depends on the composition of the material, the phase, the temperature, and whether or not it is a homogeneous material. In general terms, for homogeneous materials, the thermal conductivity goes in ascending order for gases, liquids, and solids. This is because, in that order, the separation between molecules becomes smaller, allowing energy to be exchanged more efficiently. There are marked trends according to the atomic structure of the materials. For amorphous solids, such as glass, irregularities in the atomic arrangement decrease energy transmission. For crystalline solids, whose conductivity may be higher than that of amorphous solids, energy transmission has an additional component due to the vibrational motion of the crystal lattice in the direction of heat flow. It is worth mentioning that, for the latter, imperfections in the lattice structure tend to scatter the energy-transmitting vibrations, resulting in a decrease in the ease of heat transfer. For metals, the free electrons generated by metallic bonds facilitate heat conduction, since a temperature difference causes

migration of free electrons in the direction of decreasing temperatures.

In inhomogeneous materials, properties cannot be generalized so easily. Therefore, the thermal conductivity can exhibit anisotropic behavior due to the non-regular structure of the material. For example, for porous materials, the air contained in them decreases the conductivity of the material. Therefore, the apparent thermal conductivity varies directly with the apparent volumetric density.

2.4 PTT effect

The inclusion of light in medicine has been widely exploited since the last century [9, 10]. Among the main advantages of treatments or therapies using light is the non-invasiveness, since it allows working in a localized manner. In the fight against cancer, two processes have been widely studied: photodynamic therapy (PDT) and PTT therapy (PTTT). PDT generates reactive oxygen species which kills cancer cells by apoptosis. In PTTT the excitation radiation is absorbed and subsequently converted into heat by plasmonic heating or non-radiative relaxations, which causes cell death by raising the cancer cells to over 40 °C. Particles that absorb light and subsequently interact with malignant cells to kill them are called photosensitizers [9].

As a therapy intended to be used in the human body, light in the NIR region has been widely used due to its high penetration depth. In PTT the photosensitizers are concentrated in the area of interest, to be irradiated with light which will generate a localized increase in heat and this will produce cell death. For this to work, these materials should ideally have high NIR absorption, be non-toxic and exhibit good biocompatibility. Additionally, the conversion of light to heat should be as efficient as possible.

For this purpose, several proposals have been developed, where the mechanism to

generate heat through absorption is different, among which are noble metal nanoparticles, carbon-based nanomaterials, Ln^{3+}-doped particles, etc [11–21]. Each of these systems offers its inherent advantages and disadvantages according to the process that causes the heating.

Noble metal nanoparticles, often called plasmonic nanoparticles, such as gold or silver, have been widely studied and used as photosensitizers, due to the heating generated by localized surface resonance plasmon. The free conduction electrons can be polarized through an incident resonant electric field (electromagnetic radiation). The oscillation due to the electric field produces a difference in the net charge at the boundaries of the metal nanoparticle, which leads to a significant increase in temperature. Due to the origin of the mechanism, it is crucial to know the wavelength resonant to the plasmon, which will vary in the particle according to its size or shape. This process is highly efficient in gold nanoparticles (Au NPs), due to the high light absorption, low luminescence yield. In addition, they offer the great advantage of being biologically compatible because they cannot be easily oxidized. Not only that, but there are also silver nanoparticles, which can be synthesized more easily than gold nanoparticles, but they lack good biocompatibility. Normally the absorption bands of the resonance plasmon of metallic nanoparticles are several tens of nanometers and can cover a wide region of the electromagnetic spectrum due to the physical characteristics of the particle.

When a light field is incident, the photon energy is absorbed if it is greater than the optical bandgap of the carbon-based particles. The excited electrons transfer energy to the lattice through electron-phonon coupling, which generates vibration in the material, resulting in a temperature increase at the macroscopic level. Although it is well known that thermal conduction is carried by phonons and electrons, in carbon-based materials phonons account for most of the heat conduction.

As in the case of carbon-based materials, those with Ln^{3+} as a heating element repeat the same mechanism. The Ln^{3+} ions present in the material will absorb the incident radiation (primarily materials that absorb in the NIR region have been reported), promoting electrons to excited states. These can pass to the ground state by two mechanisms, through a radiative (emission) process or non-radiative transitions. However, both processes cannot occur efficiently, in fact, there is direct competition between the two. The promotion of non-radiative processes will generate an increase in the temperature of the sample, as the excited electrons transfer energy to the matrix in which they are housed. That is why in the literature, the few examples reported as PTT materials based on processes where the protagonist is only Ln^{3+} have primarily low quantum yields, which allows an improvement in their heat conversion efficiency. Some studies report materials with high Ln^{3+} concentrations, for two reasons, the first is to increase the absorption of the material and the second is to promote more non-radiative processes that occur between ions. Most of the works reported in the literature have been in nanometric size because they are intended to be applied in biomedical approaches, so they are found in aqueous solutions. However, it has been identified that materials in solid-state, not dispersed in aqueous solution, generate a higher increase in temperature, due to the lack of means to dissipate heat. Most of the work on PTT materials using Ln^{3+} are so-called hybrids, where they are combined with other materials such as metal nanoparticles, carbon-based materials shells, etc. These significantly improve the heat conversion efficiency.

Bibliography

[1] Donald Askeland, Pradeep Fulay, and Wendelin Wright. *The Science and Engineering of Materials*. Cengage Learning, London, 2011.

[2] David Kingery, H. K. Bowen, and Donald Uhlmann. *Introduction to Ceramics*. Wiley, London, 1976.

[3] Emad El-Meliegy and Richard van Noort. *Glasses and Glass Ceramics for Medical Applications*. Springer, London, 2012.

[4] Surendranathan. *An Introduction to Ceramics and Refractories*. CRC Press, London, 2012.

[5] Wolfram Holand and George Beall. *Glass ceramic technology*. Wiley, Canada, 2012.

[6] Alan Chapman. *Transmisión del calor*. Bellisco, España, 1990.

[7] David Lide. *Handbook of chemistry and physics*. CRC Press, España, 2004.

[8] Theodore Bergman, Adrienne Lavine, Frank Incropera, and David Dewitt. *Fundamentals of Heat and Mass Transfer*. John Wiley & Sons, USA, 2004.

[9] Zhongjian Xie, Taojian Fan, Jusung An, Wonseok Choi, Yanhong Duo, Yanqi Ge, Bin Zhang, Guohui Nie, Ni Xie, Tingting Zheng, et al. Emerging combination strategies with phototherapy in cancer nanomedicine. *Chemical Society Reviews*, 49(22):8065–8087, 2020.

[10] Wenfeng Wei, Xiaoyuan Zhang, Shan Zhang, Gang Wei, and Zhiqiang Su. Biomedical and bioactive engineered nanomaterials for targeted tumor photothermal therapy: a review. *Materials Science and Engineering: C*, 104:109891, 2019.

[11] Stephan Link and Mostafa A El-Sayed. Shape and size dependence of radiative, non-radiative and photothermal properties of gold nanocrystals. *International reviews in physical chemistry*, 19(3):409–453, 2000.

[12] Hongki Kang, Jee Woong Lee, and Yoonkey Nam. Inkjet-printed multiwavelength thermoplasmonic images for anticounterfeiting applications. *ACS applied materials & interfaces*, 10(7):6764–6771, 2018.

[13] Bing Han, Yong-Lai Zhang, Qi-Dai Chen, and Hong-Bo Sun. Carbon-based photothermal actuators. *Advanced Functional Materials*, 28(40):1802235, 2018.

[14] Gururaj M Neelgund and Aderemi Oki. Photothermal effect: an important aspect for the enhancement of photocatalytic activity under illumination by nir radiation. *Materials chemistry frontiers*, 2(1):64–75, 2018.

[15] Qiyue Shao, Lilai Ouyang, Lifei Jin, and Jianqing Jiang. Multifunctional nanoheater based on nagdf 4: Yb 3+, er 3+ upconversion nanoparticles. *Optics express*, 23(23):30057–30066, 2015.

[16] Lili Feng, Fei He, Bin Liu, Guixin Yang, Shili Gai, Piaoping Yang, Chunxia Li, Yunlu Dai, Ruichan Lv, and Jun Lin. g-c3n4 coated upconversion nanoparticles for 808 nm near-infrared light triggered phototherapy and multiple imaging. *Chemistry of Materials*, 28(21):7935–7946, 2016.

[17] Kelu Zhao, Jing Sun, Fan Wang, Anyi Song, Kai Liu, and Hongjie Zhang. Lanthanide-based photothermal materials: fabrication and biomedical applications. *ACS Applied Bio Materials*, 3(7):3975–3986, 2020.

[18] Blanca del Rosal, Alberto Pérez-Delgado, Elisa Carrasco, Dragana J Jovanović, Miroslav D Dramićanin, Goran Dražić, Ángeles Juarranz de la Fuente, Francisco Sanz-Rodriguez, and Daniel Jaque. Neodymium-based stoichiometric ultrasmall nanoparticles for multifunctional deep-tissue photothermal therapy. *Advanced Optical Materials*, 4(5):782–789, 2016.

[19] Xingjun Zhu, Wei Feng, Jian Chang, Yan-Wen Tan, Jiachang Li, Min Chen, Yun Sun, and Fuyou Li. Temperature-feedback upconversion nanocomposite for accurate photothermal therapy at facile temperature. *Nature communications*, 7(1):1–10, 2016.

[20] Qian Chen, Chao Wang, Liang Cheng, Weiwei He, Zhengping Cheng, and Zhuang Liu. Protein modified upconversion nanoparticles for imaging-guided combined photothermal and photodynamic therapy. *Biomaterials*, 35(9):2915–2923, 2014.

[21] Hong Wang, Xiumei Yin, Mingming Xing, Yao Fu, Ying Tian, Xin , Tao Jiang, and Xixian Luo. Investigation on the thermal effects of nayf 4: Er under 1550 nm irradiation. *Physical Chemistry Chemical Physics*, 19(12):8465–8470, 2017.

Chapter 3

Synthesis and characterization of Sr/Zr based ceramics.

Based on the points described in the previous chapters, there is an ongoing need to improve the actual printed anti-counterfeiting technology. In this sense, and in view of the fact that temperature is not so widely used as a variable in current anti-counterfeiting technology, we noted the potential that exists in its use in the design of printed security labels.

In the present chapter, the experimental section of Sr/Zr-based PTT particles is shown. First, the composition and the synthesis method followed are described. This is followed by the structural, spectroscopic, and thermal characterization of the synthesized materials. Complementarily, a rate equation model is presented to explain the PTT behavior of the particles. Finally, the anti-counterfeiting proposal is presented, in which the PTT particles are combined with a thermochromic pigment [1].

3.1 Synthesis method: Solid-state reaction

There are a large number of reports related to the synthesis of Sr/Zr-based ceramics, as well as their structural properties and their application as thermal barrier coating materials [2–4]. In such an application, the solid-state reaction method is often used as the synthesis method because of the short time, high chemical yield and, the possibility of generating microparticles [5].

For the above described, the synthesis of Sr/Zr:Yb^{3+} ceramics was carried out by the solid state reaction method. Strontium carbonate ($SrCO_3$), zirconium oxide (ZrO_2) and ytterbium oxide (Yb_2O_3) were used as precursor compounds for the synthesis, all of them with a purity higher than 99%. In order to evaluate the PTT effect, a series of samples were fabricated in which the Sr/Zr ratio was varied and the Yb^{3+} concentration was fixed. Table 3.1 shows the label and composition of each of the fabricated samples.

Table 3.1: Parameters for the synthesis of Yb^{3+} -doped Sr/Zr hybrid oxides.

Sample	$SrCO_3$ (mmol)	ZrO_2 (mmol)	Yb_2O_3 (mmol)
PTZr	0	30.8	6.6
PTSrZr1	30.8	44	6.6
PTSrZr2	37.4	37.4	6.6
PTSrZr3	44.0	30.8	6.6
uZrO_2	0	30.8	0

The PTZr sample was based solely on ZrO_2. On the other hand, the PTSrZrX samples, (X=1,2,3) presented a variation in the Sr/Zr ratio, the first sample (X=1)

contained the highest amount of Zr^{4+}, which decreases as X increases. To demonstrate the effect of Yb^{3+} an undoped sample, uZrO_2, was processed with the same synthesis method. The stoichiometric amount of each precursor was weighed on an analytical balance (Sartorius CPDA225D, 0.00001 g),was placed in a zirconium jar to be ground in ethanol in a planetary ball mill for 4 h (MSK-SFM-1; MTI corporation). Subsequently, the slurry obtained was dried for 12 h at 100 °C. This process yielded a homogeneously distributed raw material whose particles were reduced in order to increase the area of interaction between them.

The raw homogeneous mixture was placed in an alumina crucible. Which was placed in a bench-top furnace(KSL-1700X MTI-XTL) to undergo the calcining process. The temperature was raised from room temperature to 1550 °C at a rate of 10 °C/min, to remain there for 6 h (fig. 3.1a). After this time, the temperature was allowed to drop to room temperature so that the sample could be removed from the furnace. As reported in the literature, such temperature and time allow the correct diffusion of ions, because both precursors have high melting points, the energy required for the reaction is high, mainly due to the type of bond, which is primarily ionic. The sample obtained was a powder composed of millimeter-sized grains (fig. 3.1b). For this reason, and for its characterization, the size of all the samples was homogenized with a milling process. For this purpose, each sample was individually dry milled for 30 minutes in a planetary mill (MSK-SFM-1; MTI corporation), using a jar and zirconium balls, in order to obtain a fine powder. For PTT characterization, each sample was individually pressed at 8 MPa for 10 minutes to form 0.5 g pellets with a diameter of 10 mm using an hydraulic press (EQ-YLJ-40T, MTI corporation).

Figure 3.1: (a) Crucible coming out of the furnace. (b) Example of the appearance of the samples after the sintering process.

3.2 Characterization

This section presents the results of the various characterization techniques used. The XRD technique was used to determine the crystalline structure of the samples. It is

important to maintain the same conditions in the comparison of properties, so with SEM a similar particle size was ensured among all samples. Once a similar particle size was assured, PTT evaluation was performed. Spectroscopic characterization, emission and decay time, allowed to evaluate the origin of the PTT effect in the samples, for which a rate equation model was proposed.

3.2.1 XRD

Measurement of diffraction patterns was performed over a range of 20 to 90° (D2 PHASER 2nd GEN, BRUKER) using a step of 0.02° and a scanning speed of 0.5° s^{-1}. Phase identification was performed using DIFFRAC.EVA software (BRUKER), filtering by chemical composition in the ICDD PDF-2 Release 2013 database.

All samples presented a well-defined crystal structure, which can be seen in the XRD patterns of fig. (3.2) as sharp peaks.

Fig. (3.2) shows that PTZr sample presents a cubic structure Fm-3m (Fig. 3.2a).All peaks belong to the $c - ZrO_2$ cubic structure (PDF 081-1550) and there are none related to other crystalline phases. Surprisingly, despite the large amount of Yb^{3+} present in the sample, there are no peaks associated with that element, so the cubic phase remains stable. Wang et al. reported that the $c - ZrO_2$ cubic phase is stable in the range of 8 to 40 mol% Yb^{3+} [6]. This can be explained by the fact that when large amounts of Ln^{3+} are introduced into ZrO_2, a $Ln_2Zr_2O_7$ composite with a fluorite or pyrochlore structure is usually formed [7–11]. Due to the valence difference between Zr^{4+} and Ln^{3+}, the inclusion of Ln^{3+} generates a large number of structural oxygen vacancies producing an increase in phonon scattering which in turn results in a decrement in thermal conductivity [10]. This characteristic has been extensively studied in the materials known as RE-zirconates since they present

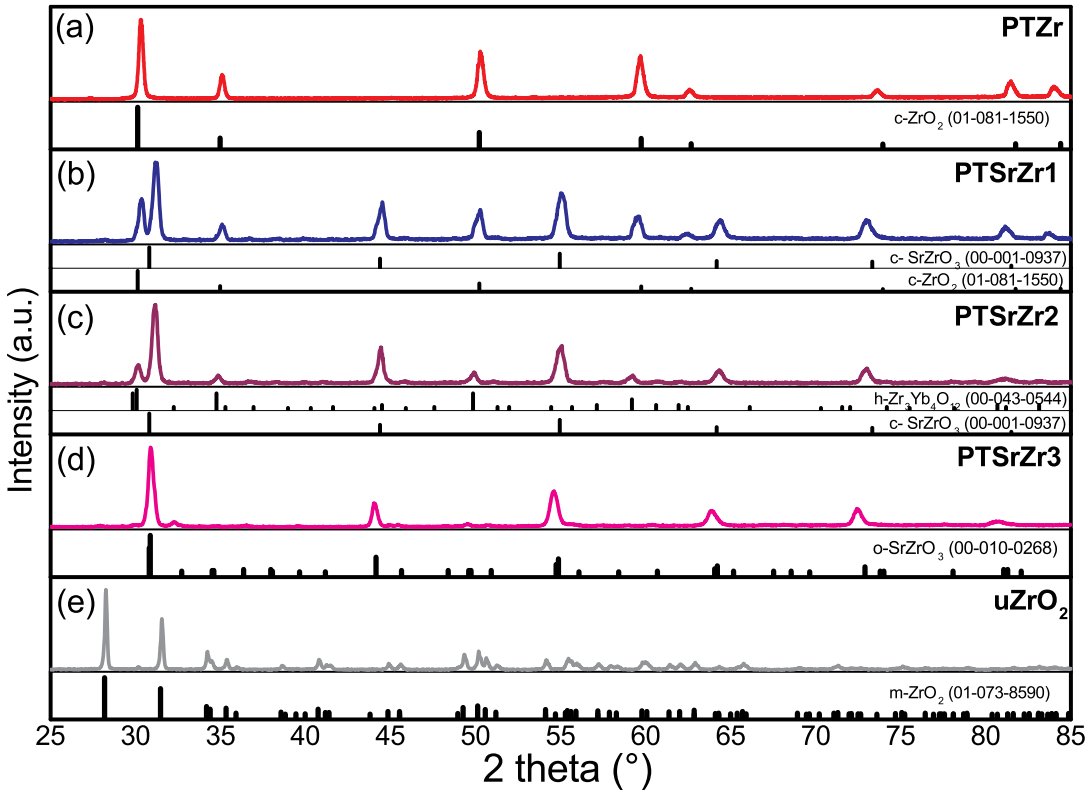

Figure 3.2: Diffractograms of the samples (a) PTZr with reference c-ZrO2 (01-081-1550), (b) PTSrZr1 with references c-ZrO2 (01-081-1550) and c-SrZrO3 (00-001-0937), (c) PTSrZr2 with references c-SrZrO3 (00-001-0937) and h-Zr3Yb4O12, (d) PTSrZr3 with reference o-SrZrO3 (00-010-0268) and (e) inert sample uZrO2 with reference m-ZrO2 (01-073-8590).

an enhanced thermal insulating capability in comparison to ZrO_2 cubic crystalline phase. Both crystal structures are structurally similar and are only distinguishable by XRD when the position of Ln^{3+} is occupied by Gd^{3+}, Sm^{3+}, Nd^{3+} or La^{3+} since new peaks appear. For this reason, it is not possible to mention that the $c - ZrO_2$ phase is the only one present in the PTZr sample since the $Yb_2Zr_2O_7$ phase can be formed. This would produce a significant reduction in the thermal conductivity since

at room temperature $Yb_2Zr_2O_7$ has a value of 1.97 W/mK, which is lower than that present in materials with the $c - ZrO_2$ phase (3 W/mK) [7, 10].

The introduction of Sr^{2+} cation induces the formation of new crystalline phases, with different thermal properties. Such is the case of the sample PTSrZr1 (fig. 3.2b), which presents the same $c - ZrO_2$ structure as PTZr but, in addition, a cubic perovskite $SrZrO_3$ crystalline phase has been formed for which a thermal conductivity value of approximately 3 W/mk has been reported [12]. Similarly, by modifying the ratio between Sr^{2+} and Zr^{4+}, new crystalline phases appear as in the sample PTSrZr2(fig. 3.2c), in which the phases $c - SrZrO_3$ and $h - Zr_3Yb_4O_{12}$ are found, for this last phase no thermal conductivity values have been reported. The PTSrZr3 sample only contains peaks related to the $o - SrZrO_3$ phase (fig. 3.2d), for which a value of 5 W/mK has been reported [4, 13]. The impact of thermal conductivities on the PTT effect of the synthesized samples will be discussed in more detail in section 3.2.4.

3.2.2 SEM

Particle size measurement was performed using a JSM-7800F SEM (JEOL). This microscope is located in a room with a controlled temperature of 20 °C and was used in a secondary electron mode configuration at a voltage of 1 kV. As a result, high-resolution images were obtained, showing the particles and a bar indicating the scale of measurement 1 μm, which were obtained under the same x5,000 magnification (fig. 3.3).

After the sintering process, a bulk material is obtained, consisting of partially bonded micrometric particles (left side of fig. 3.3). The grinding process, subsequent to sintering, only achieves the separation of the bonded particles, not their reduction,

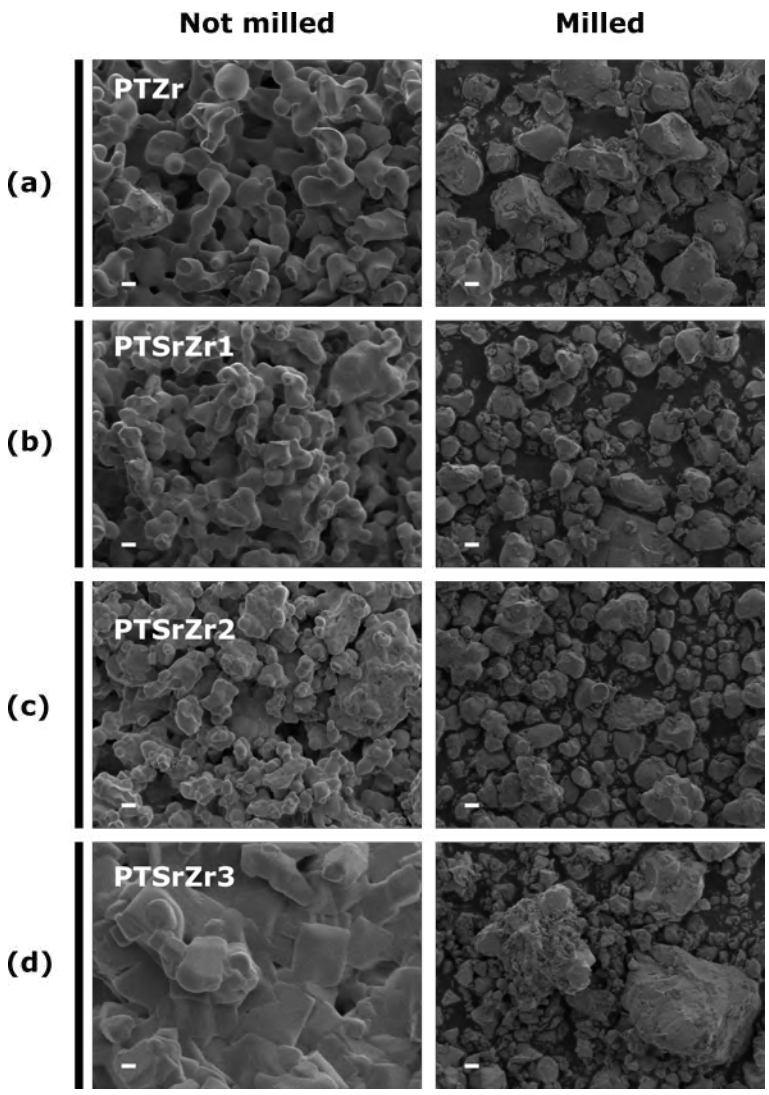

Figure 3.3: SEM images of (a) PTZr, (b) PTSrZr1, (c) PTSrZr2 and (d) PTSrZr3 samples after the sintering process (left) and after milling process (right). The scale bar indicates 1 μm.

as shown on the right side of fig. 3.3. Samples PTZr, PTSrZr1 and PTSrZr2 (fig. 3.3 a-c), before the milling process show particle junctions in the range of 1 to 5 μm, being sample PTZr the one with the highest amount of particles larger than 3 μm.

On the other hand, sample PTSrZr3 shows particle junctions of more than 6 μm, and even a complete melting of the material, which can be attributed to the fact that it is the sample with the highest concentration of $SrCO_3$, which reduces its melting point. After grinding, the size trend continues to be maintained. This is due to the fact that the hardness of the crystalline phases decreases in the following order: $o-SrZrO_3$, $c-ZrO_2$, $c-SrZrO_3$, which are present in the samples PTSrZr3, PTZr and PTSrZr1, respectively [14, 15]. For the $h-Zr_3Yb_4O_{12}$ phase, of PTSrZr2, there is no reported hardness value, but we suspect that it is similar to that of $c-SrZrO_3$, since the particle size distribution of the PTSrZr1 and PTSrZr3 samples is similar.

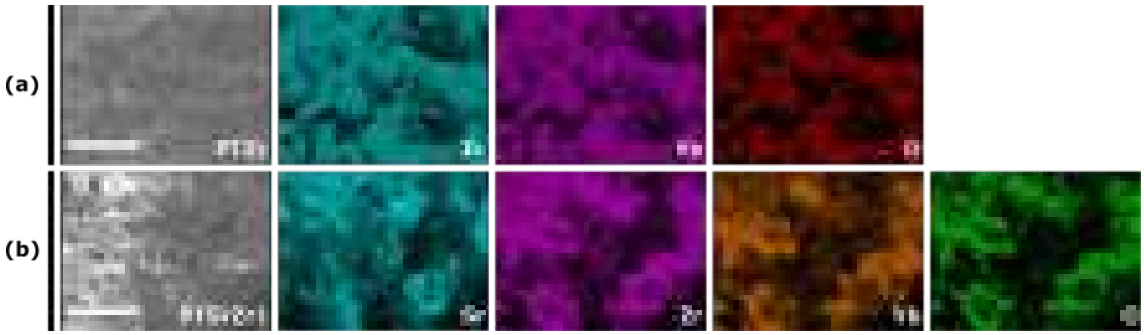

Figure 3.4: EDS mapping of (a) PTZr and (b) PTSrZr1 samples. The scale bar indicates 5 μm.

EDS analysis indicates that for the PTZr sample the distribution of elements is homogeneous, since there is only one crystalline phase. On the other hand, the PTSrZr1 sample shows a clear heterogeneity in the distribution of elements. There is a clear distinction in the areas where there is a higher concentration of Sr or Zr, which could be attributed to the two crystalline phases present in the sample. From the mapping for the PTSrZr1 sample it is not possible to say which element the Yb replaces, although it is reported in the literature that is Sr in the crystalline structure.

3.2.3 Spectroscopic characterization

Reflectance spectra measurements were performed using a Cary 5000 UV-Vis-NIR spectrophotometer (Agilent) in a range of 400 to 1400 nm in order to know the region of excitation for the PTT effect. The rate equation model requires the emission data and decay times, so they were measured using a 965 nm LD as excitation, a monochromator (Acton Instruments SP-2300i) and an InGaAs detector (Thorlabs DET10C) to collect the data. The emission spectrum was measured in the range of 980 to 1100 nm at different powers, while the decay curves were obtained by means of an HDO4054 oscilloscope (Teledyne LeCroy) and then fitted to a single exponential decay.

Fig. 3.5a shows the reflectance spectra of synthesized samples. Evidently, the main absorption band in all the samples corresponds at the transition ${}^2F_{7/2} \rightarrow {}^2F_{5/2}$ in Yb^{3+}, which is the only possible transition (fig. 3.5b) and is centered at 975 nm. That wavelength was used as excitation to measure the PTT performance of synthesized materials. It is necessary to mention that no absorption band was detected in the $uZrO_2$ sample because there is no amount of Yb^{3+} in it.

Due to the high concentration of Yb^{3+} in the samples, it was only possible to measure in the PTSrZr1, which are shown in fig. 3.6 at several 965 nm LD powers. Emission bands characteristic of Yb^{3+} can be observed, which maintain the emission profile and in turn increase in intensity with increasing power.

The transition centered at 1021 nm was used to monitor the lifetimes at different powers. As can be seen in fig. (3.7a-d), the average lifetime is 1.755 ms and it does not vary significantly with increasing power. In other words, the lifetime does not depend on the excitation power, this deduction is shown in section 3.3.1, where this will be demonstrated analytically.

3.2.4 PTT characterization

PTT characterization was carried out on the fabricated pellets, which were mounted in plastic tweezers to avoid heat dissipation. Individually and at room temperature, each pellet was irradiated for one minute with a 975 nm LD at a fixed power. After that period, with a Keysight U5855A TrueIR thermal camera, the maximum temperature reached by the sample was measured and immediately the LD path was interrupted in order to allow the sample to cool down and not to alter the LD stability. Once the sample temperature dropped to ambient, the LD power was raised and the process was renewed. This procedure can be repeated many times without significant variation in the results It is worth mentioning that the LD wavelength was far from the sensitivity of the thermal camera, so there were no alterations in

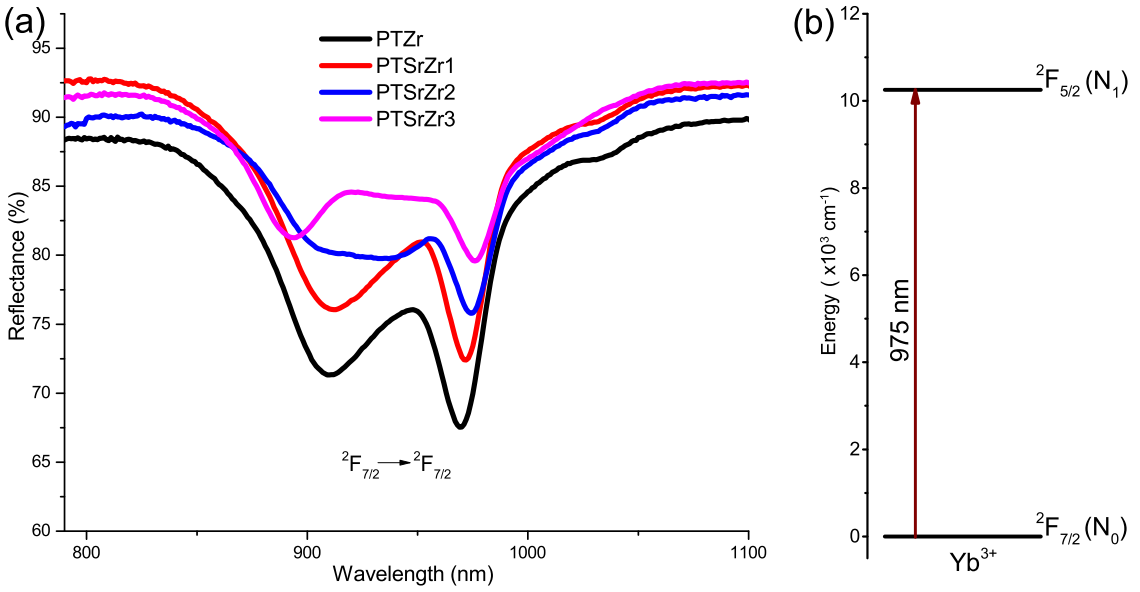

Figure 3.5: (a) Reflectance spectra of PTZr, PTSrZr1, PTSrZr2 and PTSrZr3 samples, where the only allowed (b) transition of Yb^{3+} is shown ($^2F_{7/2} \rightarrow {}^2F_{5/2}$).

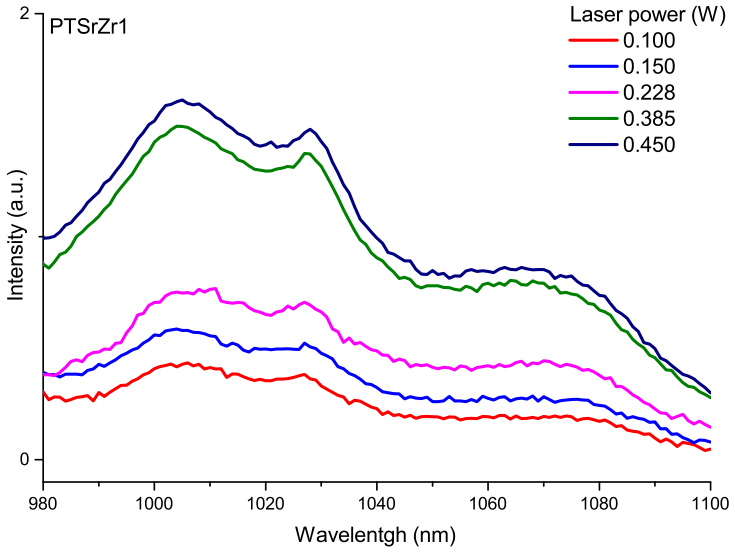

Figure 3.6: Emission spectra of PTSrZr1 sample at several power.

Figure 3.7: Decay curves of PTSrZr1 sample at several power.

the measurements.

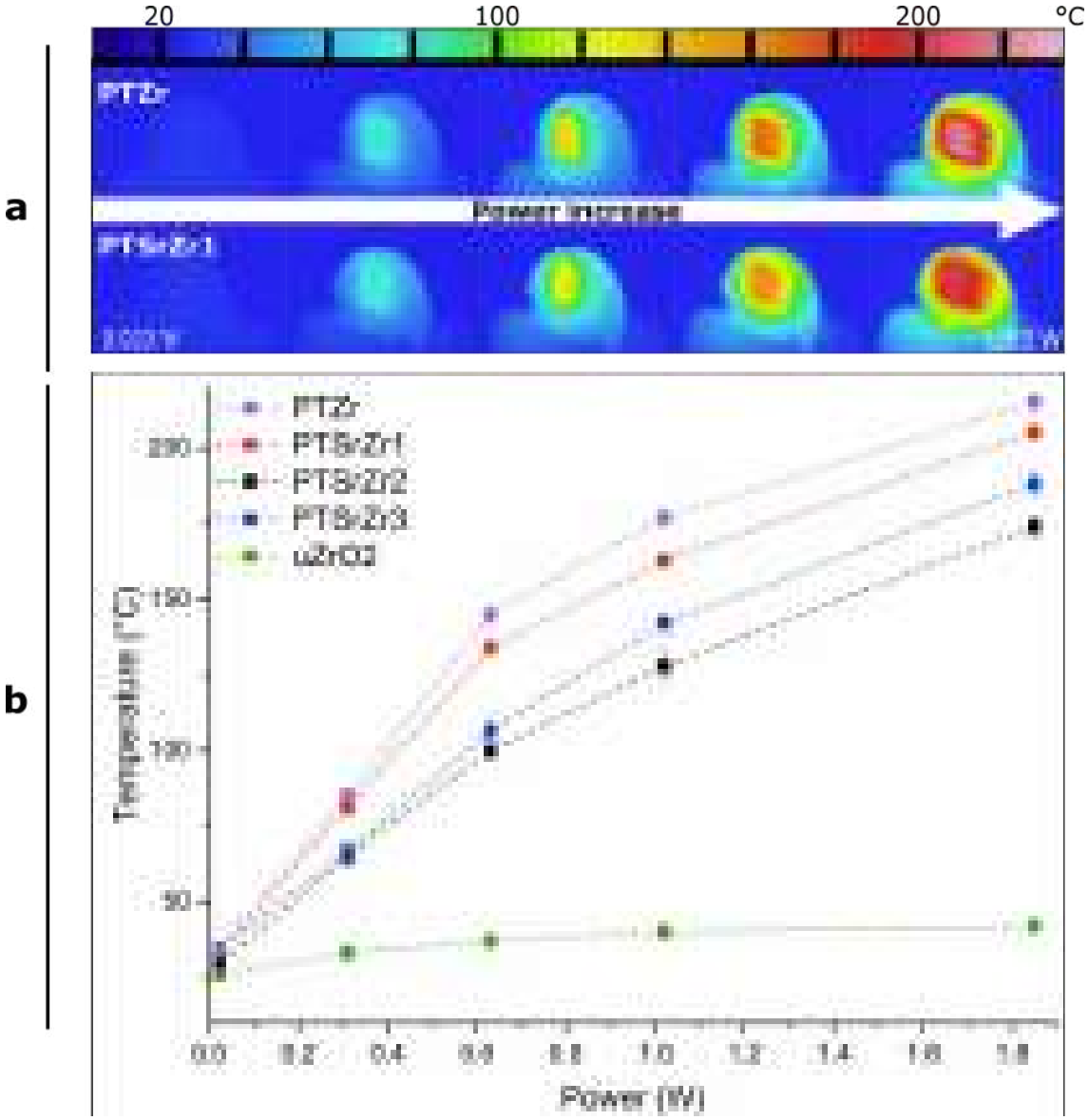

Figure 3.8: (a) Temperature images of PTZr and PTSrZr1 samples at different power irradiation of LD. (b) Maximum temperature reached after 1 min of LD irradiation of all synthesized samples.

The thermal images of Fig. (3.8a) show the heating process of PTZr and PTSrZr1 when irradiated at different 975 nm LD power. As expected, the higher the irradiation power, the higher the temperature generated by the samples. The corresponding quantitative result of the above process, for each sample, as a function of 975 nm LD excitation power is shown in fig. (3.8b). At low LD excitation powers, less than 0.1 W, the temperature in all samples does not show a significant increase and thus remains close to ambient. However, after 0.1 W, the temperature in the samples rose as the excitation power increased. The highest temperature values at each excitation power correspond to sample PTZr, followed by samples PTSrZr1, PTSrZr3 and finally PTSrZr2. For example, at 1.85 W the temperatures generated were 215, 205.4, 188.1 and 174 °C in the order given above. Clearly, as shown in fig. (3.8b), the $uZrO_2$ sample has the lowest temperature rise at all excitation powers. At maximum power excitation, 1.8 W, the temperature increases up to 42 °C that is only 17 °C more than the initial temperature, which is insignificant compared with the 180.4 °C generated by PTZr sample. That points the importance of the Yb^{3+} doping in samples, letting them able to specifically be excited by light at 975 nm. As is shown in table 3.1, the Yb^{3+} concentration was the same in all Yb^{3+} doped-samples, so the difference in temperature may be explained in terms of the differences in thermal conductivity values. As was mentioned, $c-ZrO_2$, $c-SrZrO_3$, and $o-SrZrO_3$ phases presented in PTZr, PTSrZr1, and PTSrZr3 samples, respectively, have values of 2, 3, and 5 W/mK as reported [4, 13, 16]. The value for $h-Zr_3Yb_4O_{12}$ was not found, but we suspect it is the highest because the temperature reached for the PTSrZr2 sample was the lowest at all LD excitation powers. The results show that a low thermal conductivity value promotes the generation of an increase in temperature of samples since it tends to increase rapidly as there is not a good dissipation of it. As shown in fig. 3.6, the emission intensity of the samples is very low, which is in agreement

with Wang et al. who showed that a high concentration of Ln^{3+} tends to promote non-radiative transitions [17]. This allows us to deduce that only a small fraction of the absorbed energy is converted to emission photons, which would indicate that the remaining energy is converted to heat. This process will be justified in section 3.3.1. In comparison with other materials with high Ln^{3+} concentrations reported in the literature, such as $NaYF_4 : 25Er^{3+}$ and $LaF_3 : Nd^{3+}$, the temperature generated in the synthesized samples are higher at low and high LD excitation powers [17, 18].

The dynamics of sample heating was performed only by analyzing the two samples with the highest PTT conversion efficiency, PTZr and PTSrZr1. Fig. 3.9a shows the temperature evolution on time under 1 min excitation of LD at 310 mW. When irradiation is set, the temperature starts to increase almost at the same ratio in both samples and even both exceed 40 °C after 10 s of LD irradiation. Such temperature is important for the anti-counterfeiting application that was proposed and described in section 3.4. Consistent with fig. 3.8b, the maximum temperature reached in both samples after 60 s of irradiation was approximately 80 °C. Immediately after, the LD was turned off and the cooling process was started, which was faster in the PTSrZr1 sample because it had a higher thermal conductivity value between the two samples. As described above, the PTT response measurements were repeated 30 times and no significant variations (less than 2 %) were observed. This performance is illustrated in fig. 3.9b, where three heating-cooling cycles are stable for the PTZr and PTSrZr1 samples.

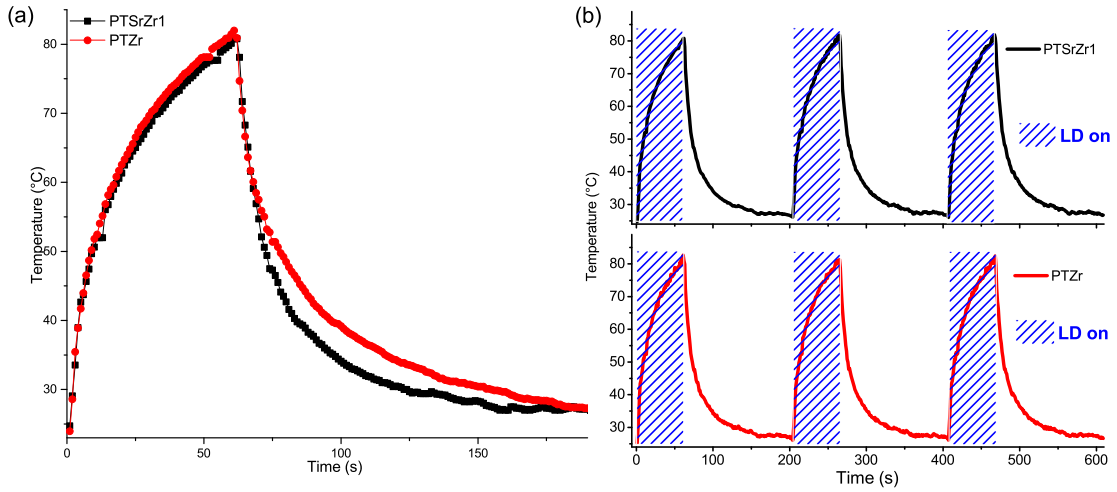

Figure 3.9: (a) Temperature of PTZr and PTSrZr1 samples as a time function and 975 nm LD (310 mW) status. (b) Temperature response of PTZr and PTSrZr1 samples during several repeated heating-cooling cycles.

3.3 Theoretical models

3.3.1 Luminescent dynamic model

In order to prove that the PTT effect is related to the low quantum efficiency of the synthesized materials, a rate equation model was proposed. Using the energy level diagram of fig. 3.5b, the luminescent dynamics can be expressed by

$$\frac{dN_1}{dt} = -A_r N_1 - W_{nr} N_0 N_1 + \varphi P N_0 \tag{3.1}$$

Where N_0 and N_1 $(ions/cm^3)$ are the population of Yb^{3+} ions in the ground $(^2F_{7/2})$ and excited $(^2F_{5/2})$ states, respectively. A_r and $W_{nr}N_0$ (s^{-1}) corresponds at radiative and non-radiative rate by concentration quenching. The last term is composed of P (W), which is the irradiation power, and φ which is the absorption

pumping rate given by

$$\varphi = \frac{\lambda}{hc\pi\omega^2}\sigma \tag{3.2}$$

where λ is the pump wavelength, ω is the radius of the pumping beam, h is the Planck constant, c is the speed of light in vacuum and σ is the absorption cross section of the transition ${}^2F_{7/2} \rightarrow {}^2F_{5/2}$. By analyzing eq. 3.1, it is possible to define the quantum efficiency (η) and the inhibition efficiency (ε) as

$$\eta = \frac{A_r}{A_r + W_{nr}N_0} \tag{3.3}$$

$$\varepsilon = \frac{W_{nr}N_0}{A_r + W_{nr}N_0} \tag{3.4}$$

The dynamic and stationary solution of eq. 3.1 are

$$N_1(t) = N_1(0)exp(-t/\tau) \tag{3.5}$$

$$N_1 = \frac{\varphi N_0}{A_r + W_{nr}N_0}P \tag{3.6}$$

From Equations 1 and 5, and what is reported in the literature, the lifetime is defined as $1/\tau = A_r + W_{nr}N_0$ and does not depend on the excitation power. The above was confirmed experimentally and shown in fig. 3.7. On average, the lifetime is $\tau = 1.755 \pm 0.021(ms)$ or

$$A_r + W_{nr}N_0 = 570 \pm 6.82(s^{-1}) \tag{3.7}$$

The emission intensity is intrinsically related to the quantum efficiency of a material, therefore they can be related as follows

$$I = C_r \eta N_1 \tag{3.8}$$

where I is the emission intensity and C_1 a constant of proportionality. Then, using eq. 3.3, for two different concentrations of Yb^{3+} is true that

$$R = \frac{I(l)}{I} = \frac{N_0(l)}{N_0} \frac{A_r + W_{nr} N_0}{A_r + W_{nr} N_0(l)} \tag{3.9}$$

where the variables with (l) correspond to those of the sample with the lowest concentration. In order to determine a value for eq. 3.9, a sample of Sr/Zr with a lower concentration of Yb^{3+} was synthesized. The emission intensity of that sample was measured, normalized and the ratio with the emission of PTSrZr1 was determined as

$$\frac{A_r + W_{nr} N_0}{A_r + W_{nr} N_0(l)} = 0.722 \pm 0.016 \tag{3.10}$$

Using the values of $N_0(l) = 6.54 \times 10^{19} (ions/cm^3)$ and, $N_0 = 7.03 \times 10^{20} (ions/cm^3)$, with eq. 3.7 and 3.9 is possible to determine that $A_r = 22.6 \pm 2.09 (s^{-1})$ and $W_{nr} = 7.80 \pm 0.47 \times 10^{-19} (cm^3 s^{-1})$.

Thus, using eqs. 3 and 4 which describe the quantum and quenching efficiencies, we have that $\eta = 0.0399 \pm 0.00611$ and $\varepsilon = 0.960 \pm 0.117$. Which, in summary, indicates that only a small amount of the absorbed energy is converted into emission photons, being mostly transformed into heat.

3.3.2 Thermodynamic model

In order to expand the understanding of the PTT effect of the material, we propose the following differential equation

$$\frac{dn_1}{dt} = -an_1 + bn_0P + an_r \tag{3.11}$$

$$n_0 + n_1 = n_m \tag{3.12}$$

where $n_0(phonons/cm^3)$ is the fundamental vibration density of the material and $n_1(phonons/cm^3)$ is the vibration density when it is subjected to LD pumping P(W). Therefore, intrinsically there must be a maximum vibration and in turn originated by the interaction with the environment, which will be denoted as $n_m(phonons/cm^3)$. $n_r(phonons/cm^3)$ is the vibration originated by the room, and $a(s^{-1})$ is the energy rate of loss or gain of the material when it interacts with the environment. The rate of conversion of the pumped energy to vibration is denoted by $b(J^{-1})$. Considering that at the macroscopic level, a vibration could be related to a temperature, eqs. 3.11 and 3.12 could be rewritten as

$$\frac{dT}{dt} = -aT + bT_0P + aT_r \tag{3.13}$$

$$\begin{aligned} T_0 + T &= T_m, \\ T(0) &= T_r \end{aligned} \tag{3.14}$$

where T, T_0, T_m and T_r (°C) are the material, minimum, maximum, and room temperature, respectively. The stationary solution of eq. 3.13, if it is considered that the excitation power does not vary with time, is

$$T = \frac{bT_mP + aT_r}{bP + a} \tag{3.15}$$

However, if we consider that the excitation power obeys a rectangular pulse that varies in time (which is how the measurements in fig. 3.8 were made) as follows

$$P(t) = \begin{cases} P_0, & 0 < t \leq t_c \\ 0, & t_c < t \end{cases} \tag{3.16}$$

where t_c is the cut-off time, where the beam is interrupted. Considering the second part of the eq. 3.14, i.e. that at time t=0 the material is in thermal equilibrium with the environment, the dynamic solution of the eq. 3.13 is

$$T(t) = \begin{cases} \frac{(T_r - T_m)bP_0 e^{-(a+bP_0)t} + bP_0T_m + aT_r}{bP_0 + a}, & t \leq t_c \\ \frac{bP_0(T_m - T_r)(e^{-a(t+t_c)} - e^{-(at+bP_0t_c)})}{bP_0 + a}, & t_c < t \end{cases} \tag{3.17}$$

Fig. 3.10 shows the results of the PTT characterization of the PTSrZr1 sample together with the data obtained with the proposed model. For the data shown it is found that $a = 0.0464s^{-1}$, $a/b = 1.521J/s$, $T_m = 348°C$ and $T_r = 27°C$

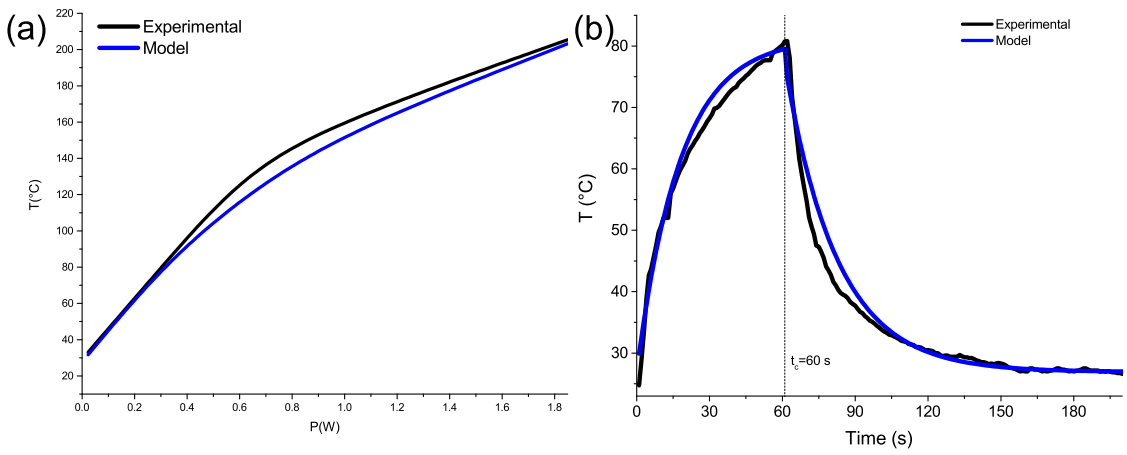

Figure 3.10: Comparison of the proposed theoretical model with the experimental results of the PTSrZr1 sample of the (a) maximum temperature reached after 60 s of irradiation and (b) the evolution of the temperature in time and state (on/off) of the 975 nm LD at 310 mW ($t_c = 60s$).

According to the results obtained, the PTZr sample presents the best PTT performance when irradiated with a 975 nm LD, so ideally (if only that effect would matter) it would be the best sample to use in the anti-counterfeiting application. However, compared to the PTSrZr1 sample, it is composed of $SrCO_3$ which is less expensive than ZrO_2, the melting point is lower (which allows for ease of synthesis) and the particle size is smaller for PTSrZr1 than for PTZr (which allows for better suspension in ink). In addition, the temperature difference between these samples is only 8 %. Therefore, it was determined to use the PTSrZr1 sample for the anti-counterfeiting application described in the following section.

3.4 Anti-counterfeiting approach based on a thermochromatic pigment

The anti-counterfeiting application has two important bases, one is the PTT effect of the PTSrZr1 sample and the other is the thermochromatic effect of a pigment (Th-P) of the Grupo Sanchez brand. The Th-P has a threshold temperature of 40 °C, below this temperature the color is black, while at higher temperatures the coloration becomes white, and this process is reversible. The damage temperature is approximately 200 °C. The proposed security system was designed to be printed, for which the inks in table 3.2 were manufactured.

In order to design the system with the highest possible security level, two different approach were designed, fabricated and tested. The approaches were manufactured using the inks of table 3.2 and following the order of figures (3.11a-b). It was ensured that the paper and acetate used as substrates in the proposals did not have absorption in NIR by means of the measurement of reflectance spectra. In such a way that

Table 3.2: Composition of the prepared inks used for printing the anti-counterfeiting approach.

Ink	**Varnish** (wt%)	**Th-P** (wt%)	**PTSrZr1** (wt%)	**uZrO$_2$** (wt%)
Th-P-ink	80	20	0	0
PT-ink	80	0	20	0
Inert-ink	80	0	0	20

with this we make sure that there would not be an affectation to the photothermic effect of the PT particles. Since the threshold temperature of Th-P is 40 °C, it was determined to use 310 mW of the 975 nm LD, since at that power the temperature of the PTSrZr1 sample is approximately 80 °C (fig. 3.8).

Fig. (3.11a) shows the first, and simplest, proposal for a printed anti-counterfeiting system. As shown, a sheet of acetate was used as substrate and a simple code (letter "M") was written on it with a conventional permanent marker. As a final layer, the code was covered with a layer formed by a combination of Th-P and PT -inks. To reveal the hidden letter it is necessary to proceed with the following effect: by irradiating the printed system with a 975 nm LD, the PTT effect of the PTSrZr1 particles is activated, thus raising its temperature. Once the temperature of the PT-ink reaches 40 °C the thermochromatic reaction of the pigment in the Th-P-ink starts, changing its color from black to white and revealing the background code. When irradiation is stopped, cooling starts and the code is hidden again. However, when subjected to a general heating of 60 °C from an hotplate, the thermochromatic effect of the Th-P-ink is activated and thus the code is revealed (fig. (3.12a)).

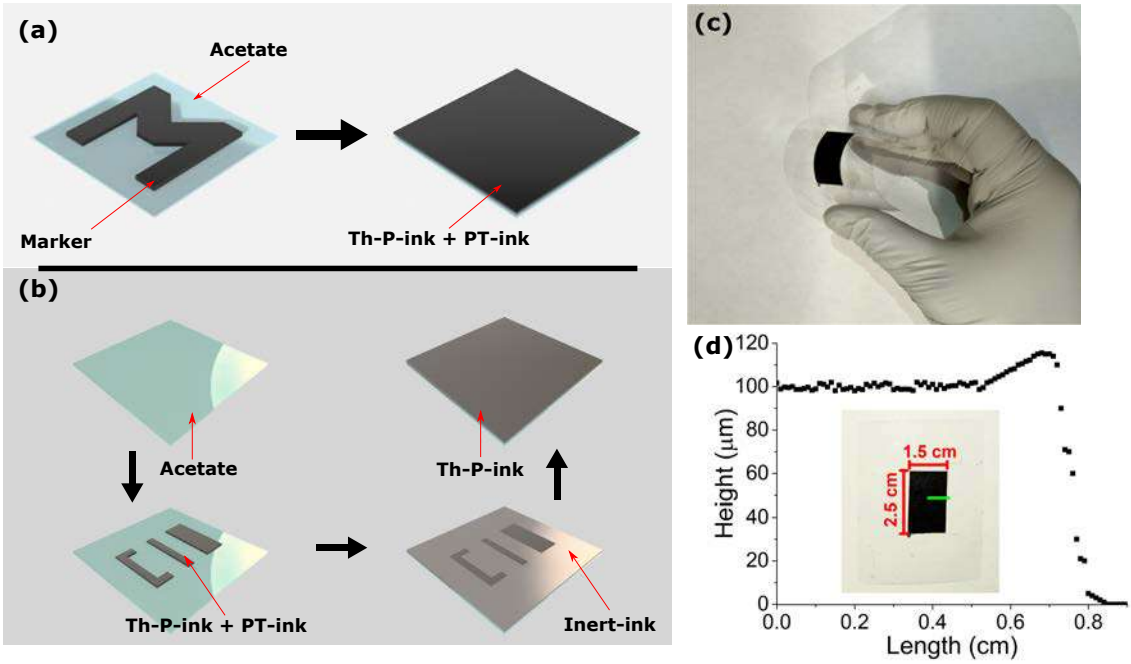

Figure 3.11: Schematics of the design of the (a) simple and (b) complex proposed systems. (c) Photograph of the second fabricated system, showing its flexibility. (d) Thickness measurement of the second fabricated system. The box shows the dimensions of the print and the green line shows the direction in which the measurement was made.

Therefore, although the proposed system does activate at a specific wavelength, the simplicity of activation by a generic heat source makes it not a good choice for a printed security system.

Fig. (3.11b) shows the design of all the layers that make up the second anti-counterfeiting proposal. On a sheet of acetate, and using PT-ink, the letters "CIO" acronym for Centro de Investigaciones en Óptica (Optics Research Center) were printed. To increase the security of the system, the second layer, with Inert-ink ink, was deposited around the first without covering it. The previous deposits were covered with a layer of Th-P-ink, in order to cover the contrast between the previous

layers. Despite containing different deposits, the system retains the flexibility of the acetate, allowing a wide range of options for future application (fig. (3.11c)). Fig. (3.11d) shows the thickness profile of the printed system, which is about 100 μm.

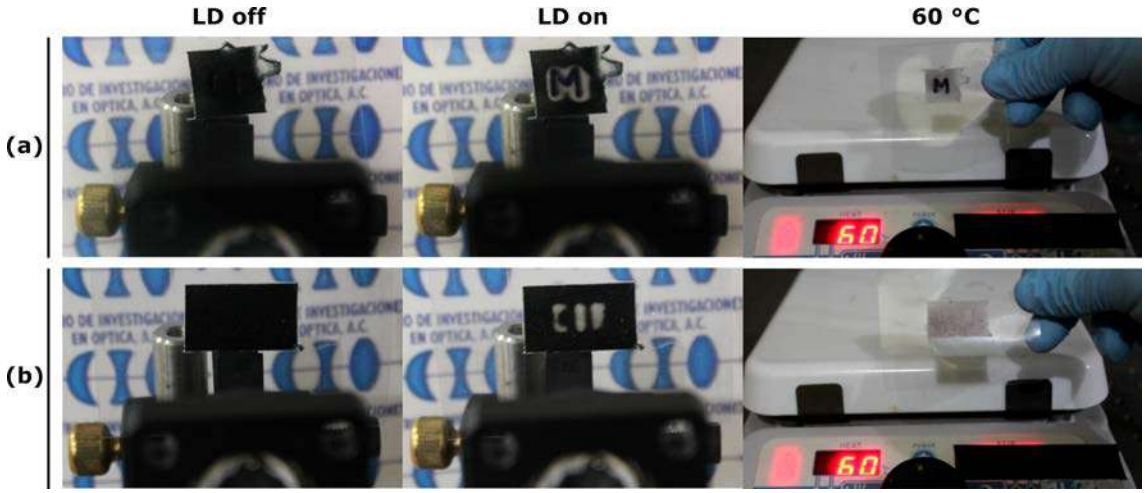

Figure 3.12: Photographs of (a) simple and (b) complex approaches with LD in mode off, on (630 mW) and under 60 °C.

The process of revealing the code in the system shown in fig. (3.11b) is initiated by irradiating the 975 nm LD. The PTSrZr1 particles, in PT-ink, absorb the LD radiation, thus activating the PTT effect described in fig. (3.8). Even if the LD radiation hits the surrounding region formed by the Inert-ink, it will not raise its temperature and will stay away from the threshold temperature of the thermochromatic pigment. Therefore, in the Th-P-ink layer, there will only be a color change in the region covering the area with the letters "CIO" (fig. (3.12b)), because it is the only region that raises its temperature when irradiated with the 975 nm LD (fig. 3.13). As described in fig. (3.5b), there is only one transition allowed in the Yb^{3+} ion, so there should be no PTT effect when irradiating the PT-ink particles with another wavelength. Therefore, irradiation with an 808 nm LD at different powers

(from 310 to 2000 mW) to the system in fig. (3.11b), did not produce a color change or code revelation. On the other hand, unlike the first proposal, if the printed system of fig. (3.11b) is placed on a hotplate at 60 °C, the color change will be homogeneous but it will not be possible to see a contrast between the first two layers (fig. (3.12b)). Therefore, the proposed system has potential to be used in printed security processes, since it maintains the restriction of disclosure to a single wavelength and, it is not susceptible to any heat source. In addition, the simplicity of printing and the accessibility of the equipment necessary for its disclosure offer advantages over the systems proposed in the literature.

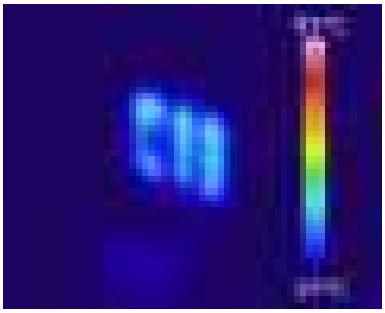

Figure 3.13: Impression temperature of the complex system when irradiated with a 975 nm LD at 310 mW. The print temperature rises to approximately 50 °C.

Bibliography

[1] Jorge Molina-González, Abril Arellano-Morales, Octavio Meza, Gonzalo Ramírez-García, and Haggeo Desirena. An anti-counterfeiting strategy based on thermochromic pigment activated by highly yb3+ doped photothermal particles. *Journal of Alloys and Compounds*, 850:156709, 2021.

[2] Leilei Sun, Hongbo Guo, Hui Peng, Shengkai Gong, and Huibin Xu. Phase stability and thermal conductivity of ytterbia and yttria co-doped zirconia. *Progress in Natural Science: Materials International*, 23(4):440–445, 2013.

[3] Zhenzhang Li, Shaoan Zhang, Qinfang Xu, He Duan, Yang Lv, Xiaohui Lin, Chuanlong Wang, Yahong Jin, and Yihua Hu. Long persistent phosphor srzro3: Yb3+ with dual emission in nuv and nir region: a combined experimental and first-principles methods. *Journal of Alloys and Compounds*, 766:663–671, 2018.

[4] Wen Ma, Daniel E. Mack, Robert Vaen, and Detlev Stover. Perovskite-type strontium zirconate as a new material for thermal barrier coatings. *Journal of the American Ceramic Society*, 91(8):2630–2635, 2008.

[5] S.-J. Cho, M.-J. Uddin, and P. Alaboina. Chapter three - review of nanotechnology for cathode materials in batteries. In Lide M. Rodriguez-Martinez and Noshin Omar, editors, *Emerging Nanotechnologies in Rechargeable Energy Stor-*

age Systems, Micro and Nano Technologies, pages 83–129. Elsevier, Boston, 2017.

[6] Hong Wang, Xiumei Yin, Mingming Xing, Yao Fu, Ying Tian, Xin , Tao Jiang, and Xixian Luo. Investigation on the thermal effects of nayf 4: Er under 1550 nm irradiation. *Physical Chemistry Chemical Physics*, 19(12):8465–8470, 2017.

[7] Jie Wu, Xuezheng Wei, Nitin P Padture, Paul G Klemens, Maurice Gell, Eugenio García, Pilar Miranzo, and Maria I Osendi. Low-thermal-conductivity rare-earth zirconates for potential thermal-barrier-coating applications. *Journal of the American Ceramic Society*, 85(12):3031–3035, 2002.

[8] Meng Zhao, Xiaorui Ren, Jun Yang, and Wei Pan. Low thermal conductivity of rare-earth zirconate-stannate solid solutions (yb2zr2o7) 1- x (ln2sn2o7) x (ln= nd, sm). *Journal of the American Ceramic Society*, 99(1):293–299, 2016.

[9] Takashi Uehara, Kichiro Koto, Fumikazu Kanamaru, and Hiroyuki Horiuchi. Stability and antiphase domain structure of the pyrochlore solid solution in the zro2 gd2o3 system. *Solid State Ionics*, 23(1-2):137–143, 1987.

[10] Qiang Xu, Wei Pan, Jingdong Wang, Chunlei Wan, Longhao Qi, Hezhuo Miao, Kazutaka Mori, and Taiji Torigoe. Rare-earth zirconate ceramics with fluorite structure for thermal barrier coatings. *Journal of the American Ceramic Society*, 89(1):340–342, 2006.

[11] Chunlei Wan, Zhixue Qu, Aibing Du, and Wei Pan. Order–disorder transition and unconventional thermal conductivities of the (sm1- xybx) 2zr2o7 series. *Journal of the American Ceramic Society*, 94(2):592–596, 2011.

[12] Baroudi Bendjeriou-Sedjerari, J Loricourt, Dominique Goeuriot, and Patrice Goeuriot. Sintering of bazro3 and srzro3 perovskites: Role of substitutions by yttrium or ytterbium. *Journal of alloys and compounds*, 509(21):6175–6183, 2011.

[13] Shinsuke Yamanaka, Ken Kurosaki, Takuji Maekawa, Tetsushi Matsuda, Shinichi Kobayashi, and Masayoshi Uno. Thermochemical and thermophysical properties of alkaline-earth perovskites. *Journal of nuclear materials*, 344(1-3):61–66, 2005.

[14] Xu-Shan Zhao, Shun-Li Shang, Zi-Kui Liu, and Jian-Yun Shen. Elastic properties of cubic, tetragonal and monoclinic zro2 from first-principles calculations. *Journal of nuclear materials*, 415(1):13–17, 2011.

[15] IR Shein, KI Shein, and AL Ivanovskii. Elastic and electronic properties and stability of srtho {sub 3}, srzro {sub 3} and tho {sub 2} from first principles. *Journal of Nuclear Materials*, 361, 2007.

[16] St Orain, Y Scudeller, and Th Brousse. Thermal conductivity of zro {sub 2} thin films; conductivite thermique des couches minces de zro {sub 2}. *International Journal of Thermal Sciences*, 39, 2000.

[17] Junxin Wang, Tian Ming, Zhao Jin, Jianfang Wang, Ling-Dong Sun, and Chun-Hua Yan. Photon energy upconversion through thermal radiation with the power efficiency reaching 16%. *Nature communications*, 5(1):1–9, 2014.

[18] Blanca del Rosal, Alberto Pérez-Delgado, Elisa Carrasco, Dragana J Jovanović, Miroslav D Dramićanin, Goran Dražić, Ángeles Juarranz de la Fuente, Francisco Sanz-Rodriguez, and Daniel Jaque. Neodymium-based stoichiometric ultrasmall

nanoparticles for multifunctional deep-tissue photothermal therapy. *Advanced Optical Materials*, 4(5):782–789, 2016.

Chapter 4

Synthesis and characterization of $LaBO_3$ based ceramics.

As mentioned in previous chapters, there are few works where the temperature is used in the decoding process in security systems and much less is the PTT effect used. Therefore, it is still a novelty to implement such processes in security printing applications.

In the present work, we show another proposal in anti-counterfeiting printed systems using PTT particles. For this purpose, $LaBO_3$ ceramic particles were synthesized and characterized structurally, spectroscopically, and photothermally. Subsequently, these were combined with a transparent vinyl varnish to be used as ink in the printing of codes, in such a way that when LD radiation is incident, images are generated and the only way to resolve them is through a thermal camera.

4.1 Synthesis method: Solid-state reaction

It was decided to use the solid-state reaction method as the synthesis procedure due to its chemical yield, the possibility of microparticle generation, and the non-generation of residues. For this purpose, the compounds boric acid (H_3BO_3) as the precursor of boron oxide (B_2O_3), lanthanum oxide (La_2O_3), and neodymium oxide (Nd_2O_3), all with a purity higher than 99 %, were used as reagents. In order to optimize the structure of the samples and at the same time to obtain an efficient PTT effect, multiple samples were fabricated, following the compositions in Table 4.1. As described, the amount of B_2O_3 was fixed at 50 mol %, while the ratio between La_2O_3 and Nd_2O_3 was varied. Individually, and for each sample, stoichiometric amounts of each precursor were weighed (Sartorius CPDA225D, 0.00001 g), and mixed in an agate mortar for 10 minutes. The mixture was then placed in an alumina crucible to be sintered, in a preheated furnace (KSL-1700X bench-top furnace, MTI corporation), at 1100 °C in air for three hours. As a result of the sintering process, partially molten micrometer particles were obtained and dry milled for 30 min (MSK-SFM-1; MTI corporation) in order to obtain a homogeneous size for PTT characterization and implementation in the anti-counterfeiting application. Pellets of 10 mm diameter were formed from each sample, by weighing 0.5 g and compressing the powder at 8 MPa for 10 min (EQ-YLJ-40T, MTI corporation), which were used to measure PTT responses.

4.2 Characterization

This section shows the results of the characterization of the fabricated $LaBO_3$ samples. The crystal structure was determined by XRD, while the particle size was

Table 4.1: Parameters for the synthesis of $LaBO_3 : Nd^{3+}$ particles.

Sample	B_2O_3 (mol%)	La_2O_3 (mol%)	Nd_2O_3 (mol%)
PTNd10	50	40	10
PTNd20	50	30	20
PTNd30	50	20	30
PTNd50	50	0	50

estimated using SEM. Both techniques allowed to estimate if the material fulfilled the necessary properties to use $LaBO_3$ as a PTT material. In order to confirm the low efficiency of the material, emission spectra were measured as a function of the concentration of the active element (Nd^{3+}). After fabrication, the PTT response was measured.

4.2.1 XRD

Measurement of diffraction patterns was performed in a range of 20 to 70° with a step of 0.02° at a time of 0.5 s^{-1} with the D2 PHASER 2nd GEN, BRUKER equipment. Phase identification and estimation of the percentage of phases were determined with DIFFRAC.EVA software (BRUKER), filtering by chemical composition in the ICDD PDF-2 Release 2013 database.

Fig. (4.1a) shows the diffractograms of the PTNdX samples (X=10,20,30,50), where it can be seen that there is no amorphous phase present. Due to the composition and fabrication parameters, all samples present, in some proportion, the orthorhombic crystal structures of $LaBO_3$ and/or $NdBO_3$ (PDF's 00-013-0113 and 00-012-0756, respectively) with a Pnma space group (62). As the concentration of

Nd^{3+} in the samples increases, the percentage of the $NdBO_3$ phase does the same while that of $LaBO_3$ decreases, as shown in fig. (4.1b). For example, in sample PTNd10 the highest concentration corresponds to the $LaBO_3$ phase, while for sample PTNd50, only the $NdBO_3$ phase is present.

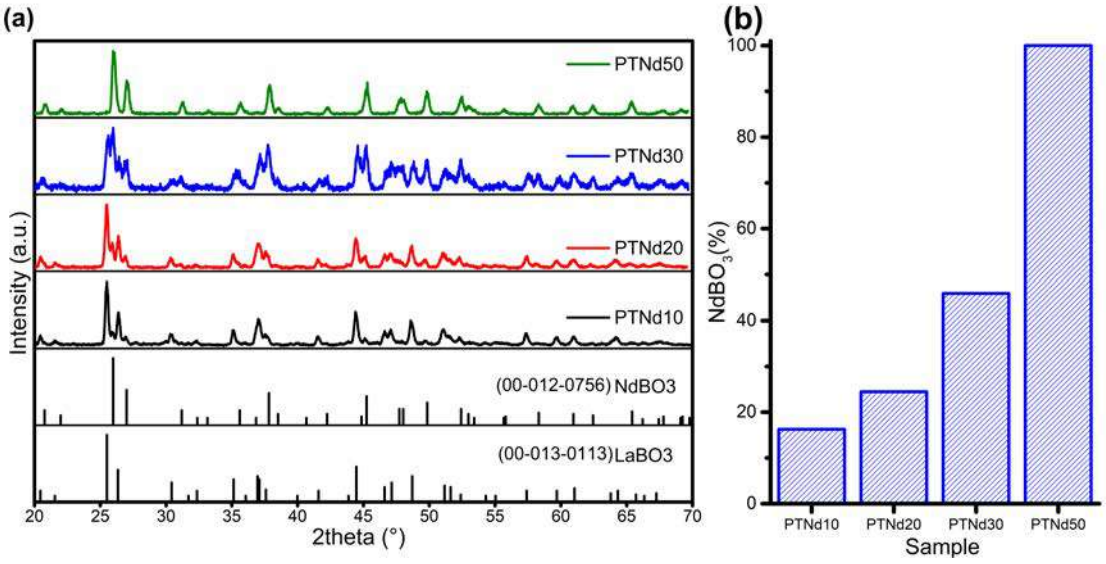

Figure 4.1: (a) XRD patterns of PTNdX (X=10, 20, 30 and 50) samples, where $NdBO_3$ (00-012-0756) and $LaBO_3$ (00-013-0113) phases are present. (b) Relative concentration of the $NdBO_3$ crystalline phase in the samples.

The crystalline phases present in the PTNdX samples belong to the family of RE borates ($REBO_3$), which have been studied for their optical and structural properties, among which stand out their transparency in the UV region, high thermal stability, and exceptional optical damage threshold [1]. However, as mentioned in section 3.2.4, a fundamental property for a PTT matrix is low thermal conductivity. $REBO_3$ family exhibits a polymorphism, determined by the radius of the RE^{3+} cation, given by orthorhombic, hexagonal, and rhombohedral structures [2–4]. It has been reported in the literature that $REBO_3$ materials with orthorhombic structures

have low thermal conductivities [5]. Therefore, having orthorhombic $LaBO_3$ and $NdBO_3$ phases, PTNdX samples have the potential to be used as PTT matrices, since low thermal conductivity means poor heat dissipation [6].

4.2.2 SEM

Since the objective of the synthesized materials is to be used in a printed system, it is essential to know the size of the particles that comprise it. Therefore, a JSM-7800F SEM (JEOL) was used. This instrument is located in a room with a fixed temperature of 20 °C and was used in secondary electron detection mode at 1kV.

Regardless of the composition, the resulting material for each of the manufactured samples is similar; a powder consisting of partially melted micrometric particles, without a defined size, and of varying size. This is because the melting point of La_2O_3 (2315 °C) and Nd_2O_3 (2233 °C) is similar, so physically the synthesis process is not drastically modified. Therefore, representative of all the samples, fig. (4.2a) shows the SEM image of the PTNd30 sample just after sintering. Similarly, fig. (4.2b) shows the EDS image of the sample, in which the distribution of the elements that make up the sample can be observed. Although each of the elements is observed distributed throughout the material, heterogeneity in the distribution is observed, mainly in the images of La and Nd. This may be since the La_2O_3 and Nd_2O_3 phases (fig. (4.1a)) may be sectionally concentrated in the sample.

In the previous chapter, it was showed the results of the synthesis of ZrO_2 and $SrZrO_3$, which requires a long synthesis process and high reaction temperatures (milling in solvent for 4 h, drying at 100 °C for 24 h, and sintering at 1550 °C for 6h) [6]. When compared to the synthesized $REBO_3$, the synthesis of the latter is shorter and the temperature required is lower, 3 h and 1100 °C respectively. In

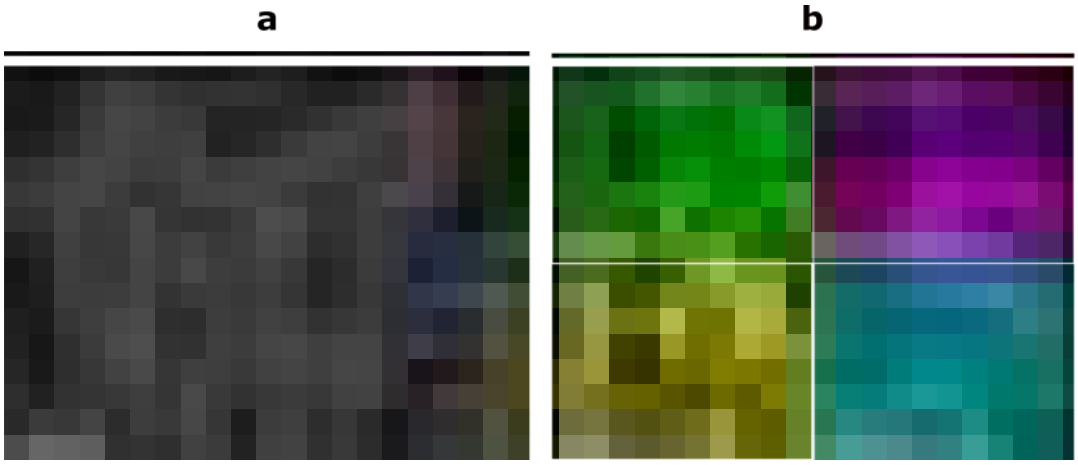

Figure 4.2: (a) SEM image and (b) EDS mapping of PTNd30 sample after sintering process.

addition, the hardness reported for the orthorhombic crystalline phase of $REBO_3$ is lower, allowing smaller particles to be obtained more easily [7–9]. Regarding the physical properties, the $REBO_3$ family has advantages to be exploited in a practical application, both for its practical production method, as well as the improvement in size reduction. This allows a better suspension in inks, thus helping to improve the printing quality.

4.2.3 Spectroscopic characterization

In concordance with the information presented in section 3.2.3, NIR reflectance spectra of the samples were performed using a Cary 5000 UV-Vis-NIR spectrophotometer (Agilent) in a range from 650 to 950 nm in order to know the NIR excitation region for the activation of the PTT effect. Emission spectra were measured to evaluate the effect of Nd^{3+} concentration in the sample. These were obtained over a range from 1000 to 1450 nm using an 808 nm LOD at 0.57 W and a monochromator (Acton

Instruments SP-2300i) coupled to an InGaAs detector (Thorlabs DET10C) to collect the data.

A new sample labeled PTNd0, which has a concentration of 0 mol% Nd_2O_3, was synthesized. This sample was occupied in the anti-counterfeiting approach, so it was also characterized. Fig. (4.3) shows the reflectance spectra of the PTNdX samples (X=0,10,20,30,50), where the absorption transitions belonging to the Nd^{3+} ion are indicated. Among these, the transitions with the highest absorption intensity correspond to ${}^4I_{9/2} \rightarrow {}^4F_{3/2} + {}^4F_{7/2}$ and ${}^4I_{9/2} \rightarrow {}^4F_{5/2} + {}^2H_{9/2}$, which are centered at 740 and 808 nm, respectively. Taking into consideration a practical application, the 808 nm LD is more commercially available and economical, so it was used as the excitation source for both photoluminescent and PTT characterization.

Emission spectra were measured in the NIR region from 1000 to 1450 nm, using 808 nm LD excitation at 0.57 W. Fig. (4.4) shows that the main emission bands are centered at 1060 and 1320 nm, which correspond to the ${}^4F_{3/2} \rightarrow {}^4I_{11/2}$ and ${}^4F_{3/2} \rightarrow {}^4I_{13/2}$ transitions, respectively. Due to the high concentration of Nd^{3+} in the synthesized samples, it was not possible to measure the emission spectra of PTNdX (X=20, 30, 50) samples, so samples with 1, 3, 4, and 5 mol % Nd^{3+} were synthesized. This is in agreement with what is reported in the literature, wherein some reports of boron-based materials with Nd^{3+} concentrations higher than 1 mol% present a drastic drop in the emission intensity [10,11]. Qualitatively it can be mentioned that the drop in emission intensity with increasing Nd^{3+} concentration means a reduction in the quantum efficiency of the material. This will mean an improvement in the PTT response of the material, as demonstrated in section 3.3.1.

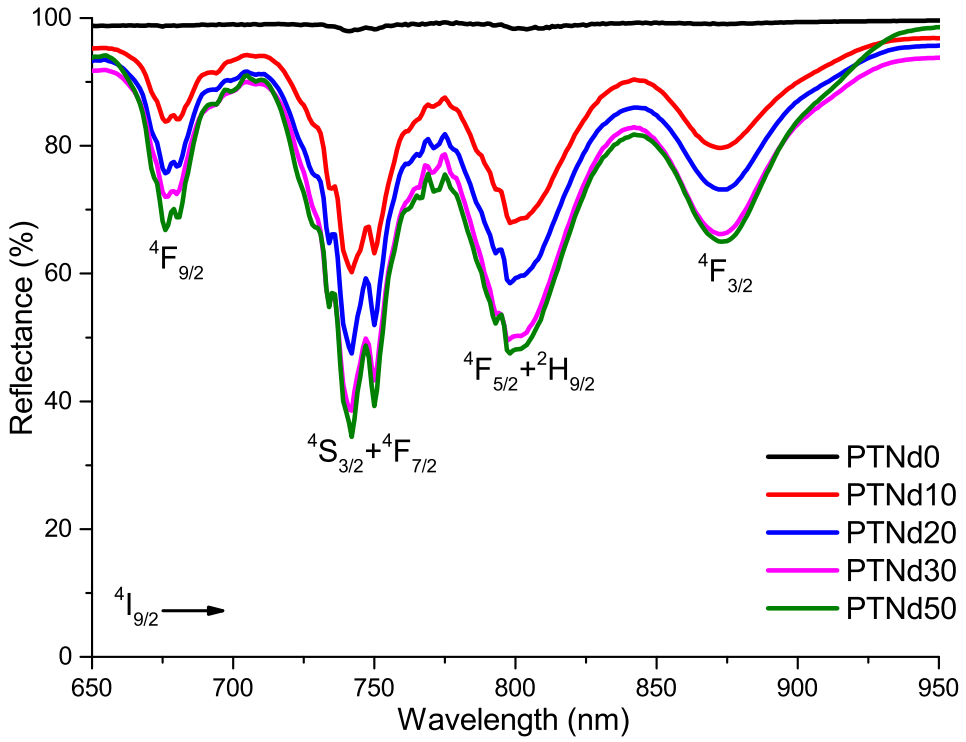

Figure 4.3: Reflectance spectra of PTNdX (X=0,10,20,30,50) samples. Transitions from the $^4I_{9/2}$ ground state to excited levels are indicated.

4.2.4 PTT characterization

The PTT characterization was performed using the same setup as described in section 3.2.4. Individually and from room temperature, each pellet of each sample was irradiated for one minute using an 808 nm LD at a fixed power. At the end of the period, the maximum temperature was recorded with the Keysight U5855A TrueIR thermal camera and immediately after that, the LD path was interrupted. When the sample temperature reached the ambient temperature, the LD power was increased, the beam path was unblocked and the process was repeated for each power.

Fig. (4.5a) shows the heating process that the PTNd30 sample undergoes as

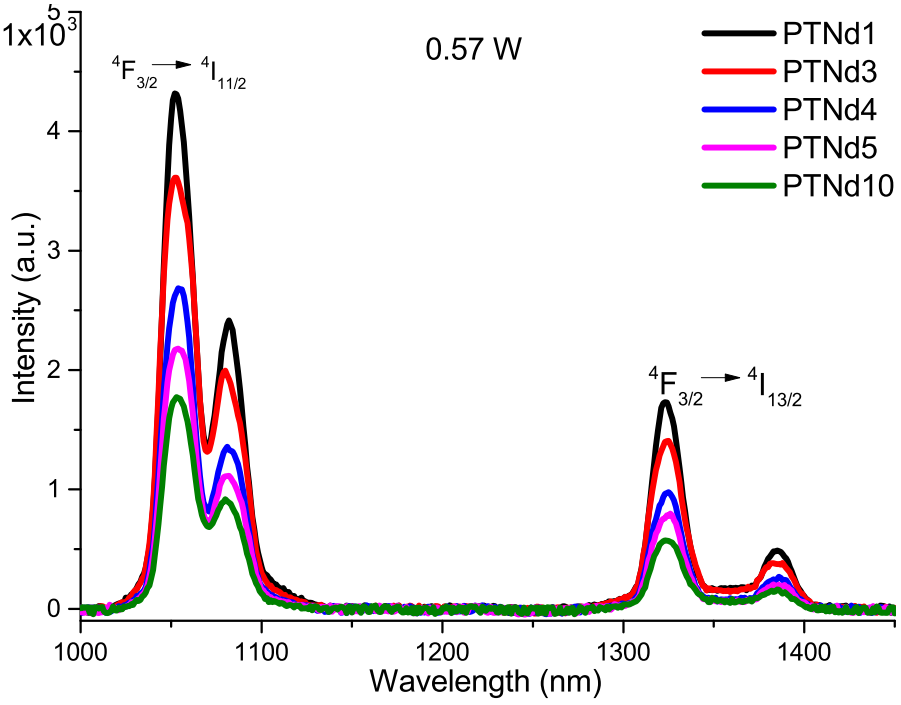

Figure 4.4: Emission spectra of PTNdX samples (X=1, 3, 4, 5 and 10) in the range of 1000 to 1450 nm at 0.57 W of 808 LD excitation.

the excitation power of the 808 nm LD is increased. The maximum temperatures recorded for each of the samples at each power are shown in Fig. (4.5b), where it can be seen that there are no significant variations for each measurement. At low irradiation powers (less than 0.015 W), the temperature in all the samples remains very close to the ambient temperature of 25 °C. However, it is clear that, as the excitation power increases, the temperature of the samples increases significantly. So much so that when excited at 2.1 W, all samples exceeded 200 °C temperature. Each measurement was repeated 30 times, i.e. each sample was irradiated 30 times at each power and there were no significant variations. This means that the samples did not suffer any damage at either low or high power, which is related to the

extraordinary optical threshold damage associated with the $REBO_3$ family [1].

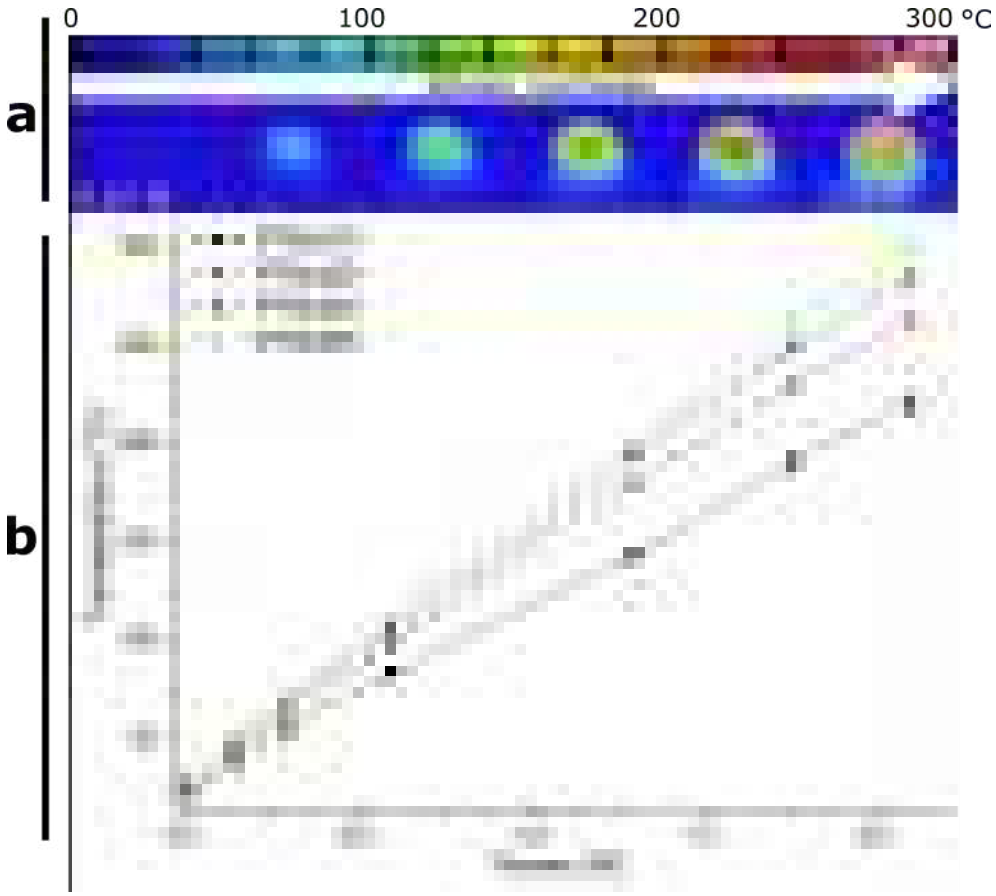

Figure 4.5: (a) Thermal images of the PTNd30 sample at different excitation powers of the LD. (b) Maximum temperature recorded after one minute irradiation of the PTNdX samples (X=10, 20, 30, 50) with the 808 nm LD at different powers.

At all excitation powers, the PTNd50 sample generates the most heating when excited with the 808 nm LD, followed by the PTNd30, PTNd20 and finally PTNd10 samples. For example, at 2.1 W the temperatures generated were 300, 284, 262 and 220 °C corresponding to samples PTNd50, PTNd30, PTNd20 and PTNd10, respectively. As mentioned in section 3.2.4, the PTT effect is highly correlated to

two parameters, low thermal conductivity and the dopant concentration. In the PTNdX samples, $LaBO_3$ and $NdBO_3$ phases are present, which are associated with low thermal conductivity [5]. Therefore, the variations in fig. (4.5b) could be fundamentally associated with variations in the concentration of Nd^{3+}, since a higher concentration increases the absorption and at the same time increases the probability of non-radiative transitions [12]. With this, the probability of photon emission decreases, which means a decrease in quantum efficiency and therefore the PTT response improves [6]. Therefore, the PTT effect predominates as the concentration of Nd^{3+} in the PTNdX samples increases.

As described in section 3.4, there is a selectivity of the PTT effect which depends on the RE^{3+} ion used in the PTT matrix. This can be seen in fig. (4.6a), where the PTNd30 sample is excited with LD 808 and 975 nm. As previously described, at 808 nm the temperature increases considerably with increasing excitation power, reaching up to 284 °C at 2.1 W. However, using 975 nm only generates heating of 37.7 °C at the same power. This is because at 975 nm Nd^{3+} does not show any absorption band. In order to demonstrate the dependence of the PTT effect on the dopant, a sample labeled PTYb30 was synthesized, which contains 30 mol% of Yb_2O_3 instead of Nd_2O_3. The only allowed transition in Yb^{3+} is centered at 975 nm (as shown in fig. (3.5b)), so by exciting at this transition it is possible to generate heating in the sample. Fig. (4.6a) shows the above, with a 975 nm LD at 2.1 W it is possible to generate heating in the PTYb30 sample of about 290 °C, which is far from the 37.5 °C generated when exciting with an 808 nm LD at 2.1 W. This important feature of the synthesized materials shows the selectivity of the PTT effect, which can be used as a security element in the anti-counterfeiting printed proposal.

As shown in fig. (4.5b), the heating of the samples is directly related to the excitation power. However, the power also has a relationship to the heating rate

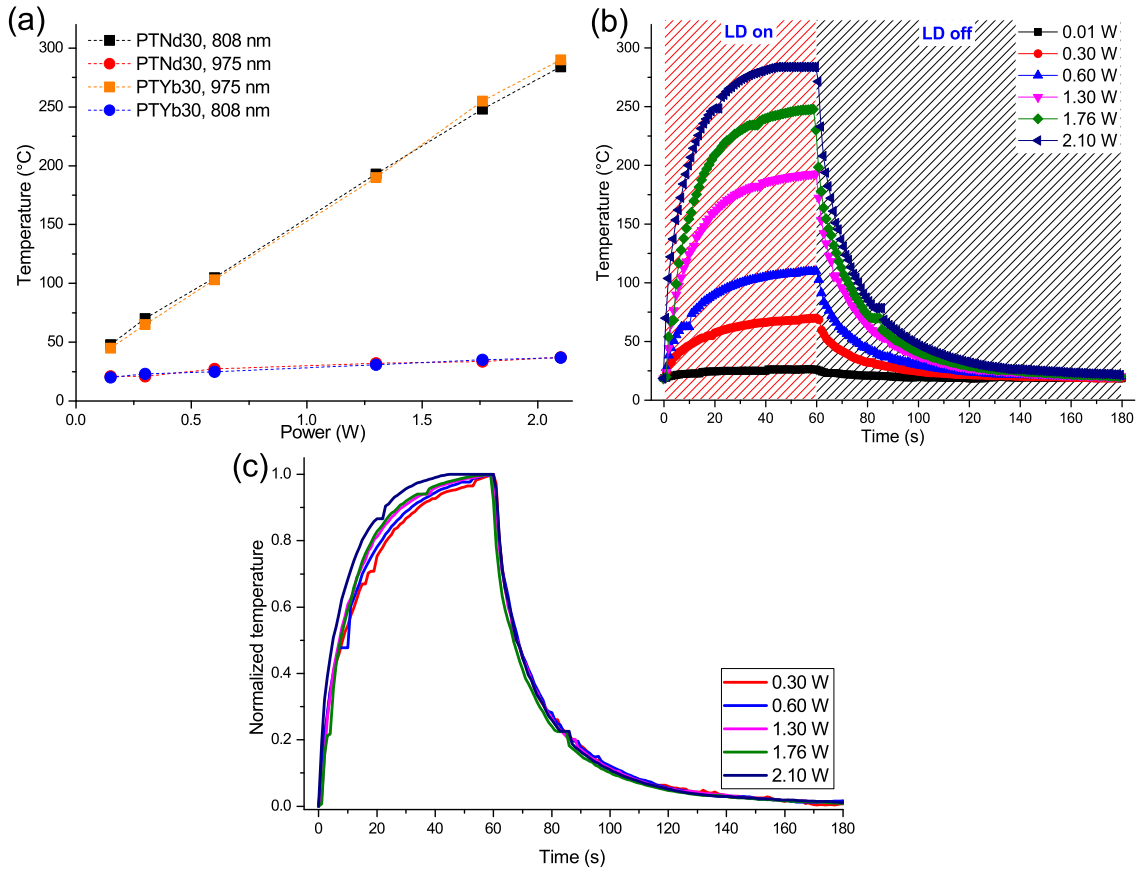

Figure 4.6: (a) Comparison of maximum temperature reached by the PTNd30 and PTYb30 samples upon 1 min of 808 or 975 nm LD irradiation. (b) Temperature of the PTNd30 sample over time as a function of the state (on or off) of the 808 nm LD. (c) Normalized temperature of PTNd30 sample at different 808 nm LD excitation power.

of the samples. In order to elucidate the above, the temperature evolution in the PTNd30 sample was measured as a function of the state (on/off) of the 808 nm LD at different powers, which is shown in fig. (4.6b). When the LD is turned on, heating occurs and when it is turned off, subsequent cooling occurs, which happens regardless of the excitation power. However, by normalizing the measurements in fig. (4.6b), it can be seen that the heating rate, i.e. the rise time, is reduced at high powers, while

the cooling (falling time) does not show significant variation (fig. (4.6c). Since being the same sample, PTNd30, there is no change in composition or properties (Nd^{3+} concentration and thermal conductivity are the same), the only parameter to which the rise time variation can be associated is the pumping power. In other words, increasing the excitation power increases the number of photons interacting with Nd^{3+} and hitting the sample, which in turn generates a change in the heating rate. In the cooling process, while the LD is off, there are no significant changes because this only depends on the environment. If a fast response time is required within the proposed anti-counterfeiting system, a high excitation power would certainly be best. However, when considering the feasibility, this would imply a great risk to the users of the system in real conditions. Therefore, a compromise between a fast response time and a sufficiently high temperature according to the design of printed system is necessary. With these considerations, it was decided to use 0.150 W of power, which is sufficient to achieve a thermal image in the anti-counterfeiting approach (to be discussed in more detail in section 4.3).

The results presented in this section show that all PTNdX samples present a more efficient PTT conversion than reported matrices with the same effect, such as $SrZO_3$ and $NaYF_4$ [6, 13, 14]. This is noteworthy since at lower excitation powers they reach similar temperatures. Comparing the results obtained in the previous chapter and the present one, the PTNdX samples, in addition to their superior PTT effect, show advantages such as cheaper precursors, shorter synthesis times, and lower sintering temperatures. Therefore, considering oxide matrices to generate a PTT effect, PTNdX samples are overall better. As shown in fig. (4.5b), the PTNd50 sample generates the highest temperature upon excitation, being the maximum difference of 5, 12, and 26 % with the PTNd30, PTNd20, and PTNd10 samples at 2.1 W. However, this sample is also the one containing the highest amount of Nd^{3+},

which means that it is the most expensive to synthesize. Therefore, understanding the trade-off between PTT response and synthesis price, the PTNd30 sample was selected to implement the anti-counterfeiting system based on thermal imaging.

4.3 Anti-counterfeiting approach based on thermal images

Similar to that described in section 3.4, the anti-counterfeiting system developed in this chapter is based on the PTT effect generated by PTNd30 particles. However, it focuses on the generation of contrast-generated thermal images acquired by the Keysight U5855A TrueIR thermal camera. As a printing method, screen printing was used, since, in addition to the simplicity and economy of the system, it offers the possibility of a large number of prints per hour [15]. For this purpose, the AT 25PA (ATMA) equipment was used, which allows to regulate the speed and the pressure of dragging, which were kept fixed in all the prints made. To make the prints, different inks were prepared, with the compositions shown in table (4.2), for which a Grupo Sanchez vinyl varnish was used as support. The designed system was implemented using a matrix of dots so that each of them functioned as a variable. Fig. (4.7) shows the negative of the design as well as the mesh used for printing. Each of the dots had a diameter of 1 mm, which coincides with the spacing between them. To exemplify, but not to be restricted to, a design of 5x11 dots (9x21 mm^2) was used. Each point can function as a variable or can be combined in order to make the design more complex. Using the advantages of the printing method, the hidden codes were printed on various substrates, including paper, acetates, banknotes, and more.

The first approximation of the system based on thermal imaging is shown in fig.

Table 4.2: Parameters of the inks manufactured for the anti-counterfeiting proposal.

Ink	**Vinyl Varnish** (wt%)	**PTNd0** (wt%)	**PTNd30** (wt%)	**PTYb30** (wt%)
Inert-Ink	80	20	0	0
PTNd-ink	80	0	20	0
PTYb-ink	80	0	0	20

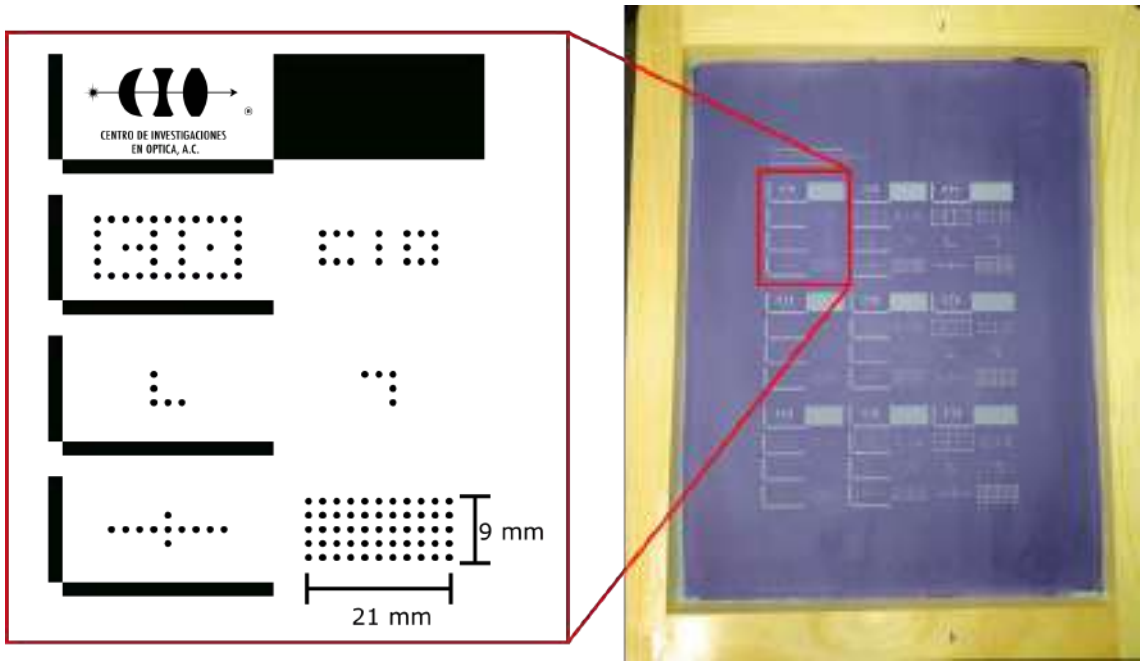

Figure 4.7: Negative used for prints where the 55-dot matrix dimension is indicated. It also shows the mesh used for printing.

(4.8). It shows how, individually, PTNd-ink and PTYb-ink were used. In design (a) there is an 11-dot cross printed on acetate and as a second layer, the 55 dots of Inert-ink in order to hide the code. When irradiated with 808 nm LD at 0.150

W the PTNd30 particles begin to heat up to approximately 48 °C, and through the thermal camera, and by the contrast between the ambient temperature, the image of the cross is generated (fig. (4.8a2)). Only the 55 dots can be seen with the naked eye (fig. (4.8a3)). In fig. (4.8b1), the first layer consists of the letters "CIO" printed with PTYb-ink and covered with 55 dots of Inert-ink. When excited at 975 nm LD at 0.150 W, the heating of the PTYb30 particles generates the thermal image where the dots of the hidden code can be seen (fig. (4.8b2)). Again, with the naked eye, it is only possible to distinguish the 55 Inert-ink dots (fig. (4.8b3)).

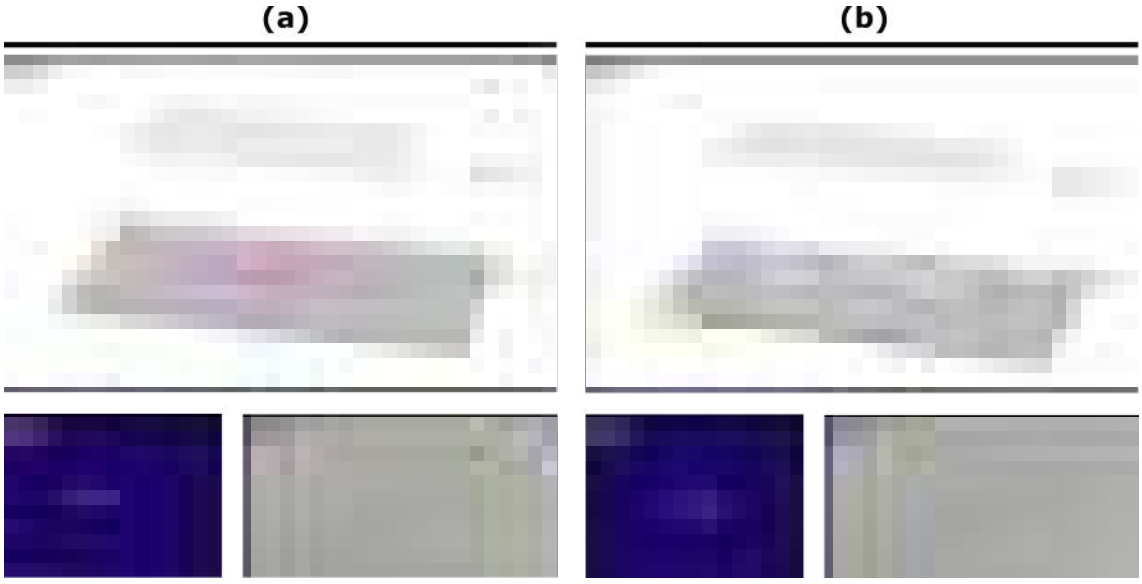

Figure 4.8: **(a)** Printed system using only PTNd-ink and Inert-ink. (1)Layer design printed on acetate, Image at (2) thermal camera and (3) naked eye upon excitation of the system at 808 nm. **(b)** Printed system using only PTYb-ink and Inert-ink. (1)Layer design printed on acetate, Image at (2) thermal camera and (3) naked eye upon excitation of the system at 975 nm.

The second approach involves a higher complexity since PTNd-ink and PTYb-ink were combined, thus exploiting the selective character of the synthesized PTT

particles. Fig. (4.9a) shows the scheme of the anti-counterfeiting design, combining the manufactured inks, and in which the order of the layers printed on acetate is indicated. The first layer consists of an "L" formed by 5 dots of PTNd-ink, while the second layer was composed of an inverted "L" of 5 dots but of PTYb-ink. To cover the previous layers, 55 dots of Inert-ink were deposited on the third layer. As previously mentioned, the printed system offers the versatility of deposition on various substrates, as shown in fig. (4.9b-c), which are photographs of the code in fig. (4.9a) on paper and acetate. As can be seen, it is only possible to define the 55-point matrix and not the first two layers. Although the design includes several layers, this does not reduce the flexibility of the substrate (fig. (4.9d)), since the final thickness of the deposits is 15 μm approximately (fig. (4.9e)).

Unlike the simple codes, which were only developed using a single excitation wavelength, in the disclosure of fig. (4.9a) the 808 and 975 nm LDs are involved, thus generating a revelation sequence. Fig. (4.10) shows the revealed sequence, where the images with single and simultaneous excitation are shown. Using the thermal camera, with the 808 nm LD, the "L" of the first layer printed with PTNd-ink is shown, while with 975 nm only the inverted "L" of the second layer is shown. Upon simultaneous excitation of 808 + 975 nm, the image generated is that of a square with 3 dots per side. In all three excitation cases, both the substrate and the Inert-ink printed dots were maintained without temperature increases, which allowed the formation of the three thermal images cases. In the three instances, it is only possible to see with the naked eye the dots that make up the 55-dot array, since all decoding happens through the thermal camera, restricting the development to that channel only. As mentioned in section 4.2.4, a trade-off between heating rate and temperature is required, and although the particles are immersed in varnish, the image is displayed about 3 s after excitation has started. This indicates that the varnish does not affect

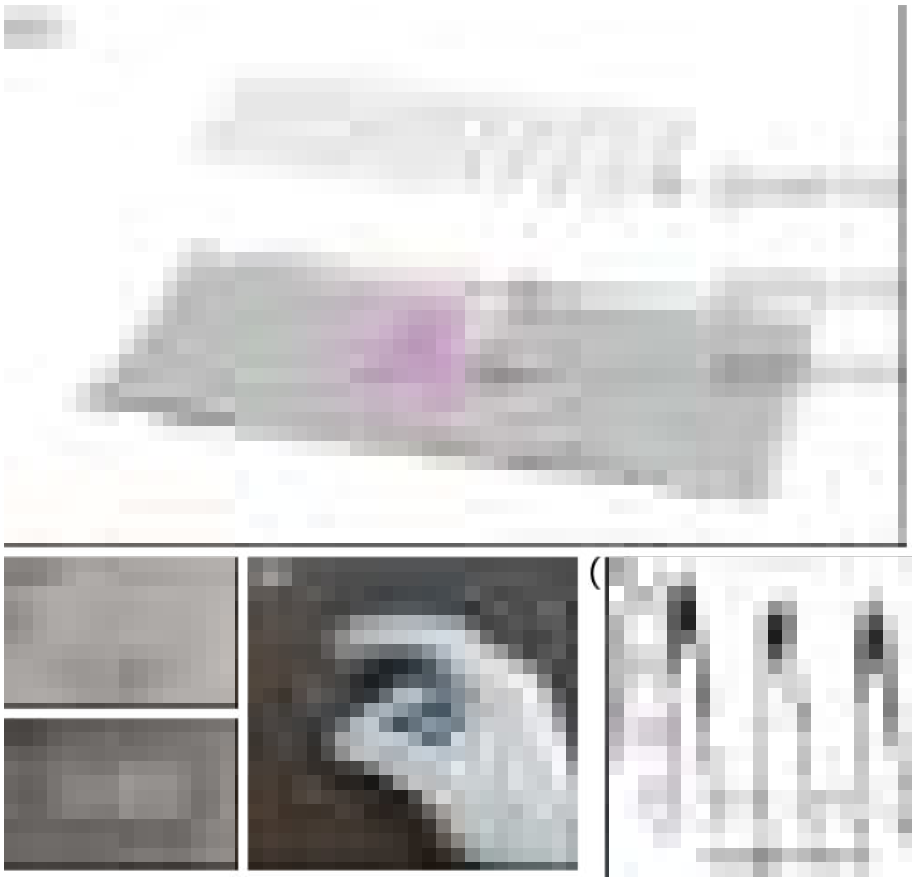

Figure 4.9: (a) Diagram of the proposed system showing the order of the layers and the ink used in each one. The colors used in the scheme are merely illustrative and were selected to differentiate each of the layers. (b) Printing of the system on paper (indicated in red box), the size is indicated as well as the path for thickness measurement (green line). (c) Printing on acetate. (d) Image of the complex system, showing the flexibility of the deposited layers. (e) Thickness of the proposed system.

the PTT response. As mentioned above, the selection of a low excitation power is for the safety of the user, however, it was also determined because at high excitation powers the dots that make up the images lose resolution. This may be the case that the individual character of the dots is lost or that even excessive heating generates

unreadable spots. The proposed system allows the resolution of a code using specific wavelengths in the NIR region, it has the particularity of being wavelength-selective and requires a thermal camera for its implementation. This offers different levels of security, which are adaptable to the specifications and requirements of a product.

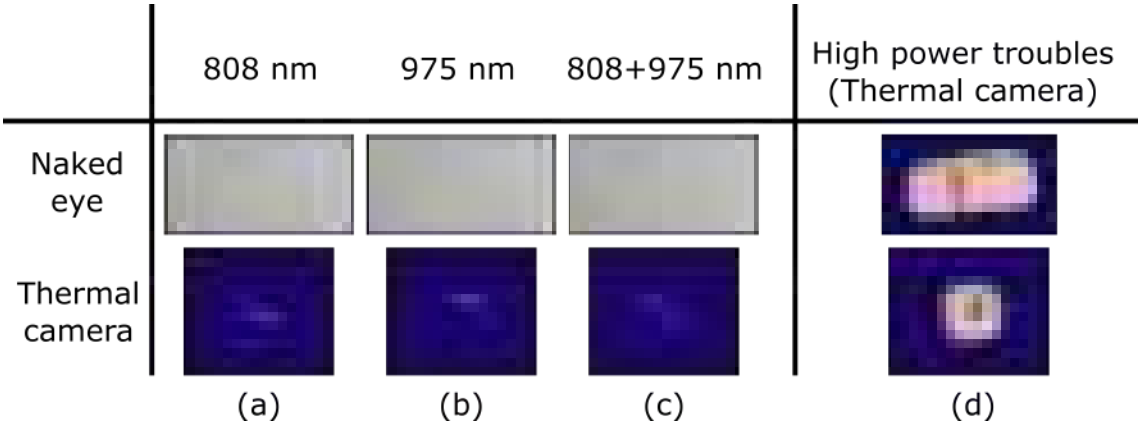

Figure 4.10: Disclosure sequence with the naked eye and thermal imaging of the printed system under an excitation of (a) 808 nm, (b) 975 nm and (c) 808 and 975 nm. (d) Examples of the effects of using high excitation powers in printed systems.

To increase the security levels in the anti-counterfeiting system and to take advantage of pumping, micrometric $NaYF_4 : 20Yb^{3+}/3Er^{3+}$ green upconversion emission particles, commercially available from Sigma Aldrich, were added. Similar to the PTT inks in Table 4.2, the upconversion particles were added to a vinyl varnish at a concentration of 20 wt% to form the UPC-ink. The design and order of the layers printed with the new ink are shown in fig. (4.11a), in which all the manufactured inks have been combined in order to illustrate the potential of the proposed system. The first layer, printed with PTNd-ink, forms a 5-dot "L", while the second layer, printed with PTYb-ink, is the inverted "L". The third layer was printed with UPC-ink and consists of an 11-dot cross. Finally, on top of all the layers, the 55-dot matrix was

printed with Inert-ink. Since the inks were combined, the hidden code will be revealed by following a sequence with the excitations (fig. (4.11b-d)). When the print is irradiated with 808 nm, visibly no information is available, while in the thermal camera the "L" of the first layer is shown. When excited with 975 nm the inverted "L" of the second layer can be seen in the thermal camera and simultaneously visibly (in green color) the cross of the third layer is visible. Simultaneous excitation of 808 and 975 nm LD shows the 3-dot square per side in the thermal camera and the cross with a visible emission. The system offers higher levels of security since it combines the thermal (PTNd+PTYb inks) and visible channels, and both excitation LD are used for its decoding sequence.

As a proof of concept, a system was designed, printed, and tested on a cardboard medicine package. The first layer, which contains the information for the thermal channel, was printed with PTNd-ink in a 5-point inverted "L" shape. The second layer was printed using UPC-ink and with the "CIO" information, which will serve for the visible channel. And as has been done up to this point, the third layer was printed with Inert-ink. The revelation sequence follows the next order, with 808 nm only the five dots of the inverted "L" are shown in the thermal camera, with 975 nm only the letters "CIO" are visible, and with the simultaneous excitation, both images are generated in their respective channels. As this is a commercial product, the cardboard used is generic for such use and, as can be seen, does not generate noise or modify any image. As illustrative, but not restrictive examples, different use cases of the system printed on medicine boxes, banknotes, and business cards are shown. The above examples are made of different materials, which do not affect the printing, sharpness, or development of the codes, so the proposed system has the potential to be used in these and other products.

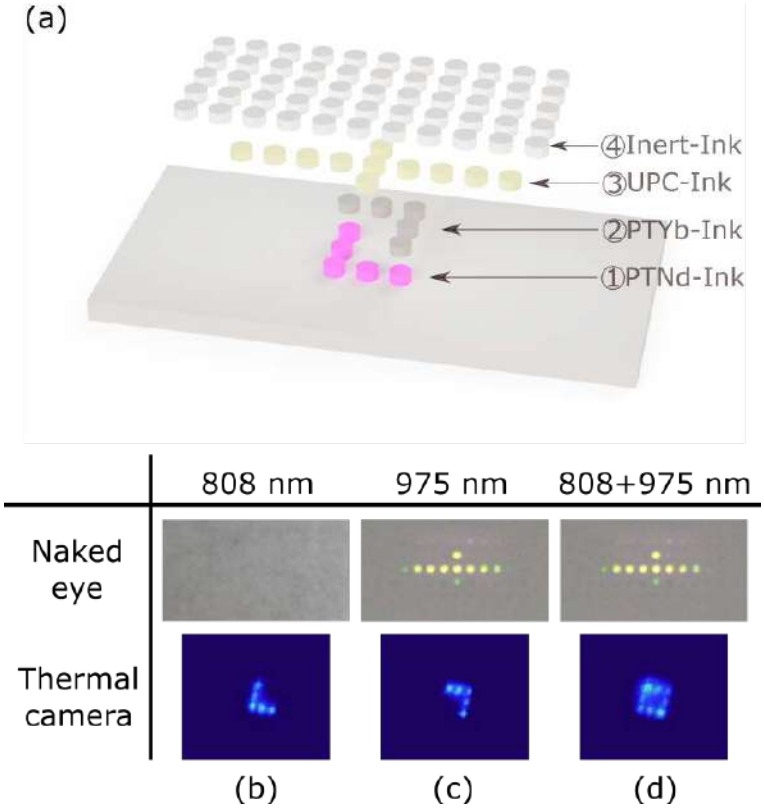

Figure 4.11: (a) Diagram of the system based on thermal and visible image. Disclosure sequence with the naked eye and thermal imaging of the printed system under an excitation of (a) 808 nm, (b) 975 nm and (c) 808 + 975 nm.

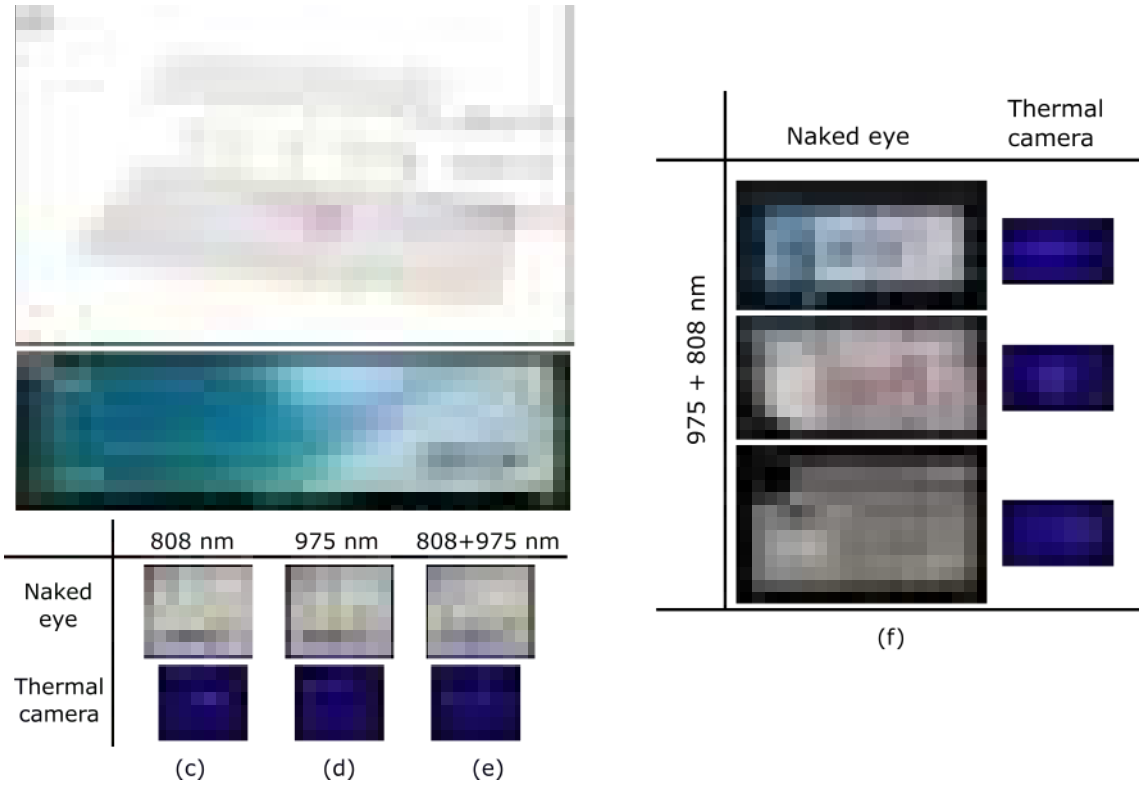

Figure 4.12: (a) Diagram of the system based on thermal and visible imagen printed on an interferon beta box. (b) Photograph of the interferon beta box indicating the security system in the red box and the dimension of the box. Sequence of naked-eye and thermal image disclosure of the printed system under (c) 808 nm, (d) 975 nm and (e) 808 and 975 nm. (f) Examples of the application of the security system based on upconversion emission and thermal imaging on different substrates, such as medicine boxes, banknotes or business cards.

Bibliography

[1] Hubert Huppertz. Multianvil high-pressure synthesis and crystal structure of β-ybbo3. *Zeitschrift für Naturforschung B*, 56(8):697–703, 2001.

[2] Y Laureiro, ML Veiga, F Fernandez, R Saez Puche, A Jerez, and C Pico. Synthesis, characterization and magnetic properties of lnbo3 (ln≡ nd, gd, tb, dy, ho and er). *Journal of the Less Common Metals*, 157(2):335–341, 1990.

[3] S Lemanceau, G Bertrand-Chadeyron, R Mahiou, M El-Ghozzi, JC Cousseins, P Conflant, and RN Vannier. Synthesis and characterization of h-lnbo3 orthoborates (ln= la, nd, sm, and eu). *Journal of Solid State Chemistry*, 148(2):229–235, 1999.

[4] Ernest M Levin, Robert S Roth, and Jerry B Martin. Polymorphism of abo3 type rare earth borates. *American Mineralogist: Journal of Earth and Planetary Materials*, 46(9-10):1030–1055, 1961.

[5] B Steele, AD Burns, A Chernatynskiy, RW Grimes, and Simon R Phillpot. Anisotropic thermal properties in orthorhombic perovskites. *Journal of materials science*, 45(1):168–176, 2010.

[6] Jorge Molina-González, Abril Arellano-Morales, Octavio Meza, Gonzalo Ramírez-García, and Haggeo Desirena. An anti-counterfeiting strategy based

on thermochromic pigment activated by highly yb3+ doped photothermal particles. *Journal of Alloys and Compounds*, 850:156709, 2021.

[7] A Jain, AK Razdan, PN Kotru, and BM Wanklyn. Load and directional effects on microhardness and estimation of toughness and brittleness for flux-grown labo 3 crystals. *Journal of materials science*, 29(14):3847–3856, 1994.

[8] Hanzheng Guo, Jing Guo, Amanda Baker, and Clive A Randall. Cold sintering process for zro2-based ceramics: significantly enhanced densification evolution in yttria-doped zro2. *Journal of the American Ceramic Society*, 100(2):491–495, 2017.

[9] Yuchen Liu, Bin Liu, Huimin Xiang, Yanchun Zhou, Hongqiang Nian, Hongfei Chen, Guang Yang, and Yanfeng Gao. Theoretical investigation of anisotropic mechanical and thermal properties of abo3 (a= sr, ba; b= ti, zr, hf) perovskites. *Journal of the American Ceramic Society*, 101(8):3527–3540, 2018.

[10] Lauro JQ Maia, Andre L Moura, Vladimir Jerez, and Cid B de Araújo. Structural properties and near infrared photoluminescence of nd3+ doped ybo3 nanocrystals. *Optical Materials*, 95:109227, 2019.

[11] J Mascetti, C Fouassier, and P Hagenmuller. Concentration quenching of the nd3+ emission in alkali rare earth borates. *Journal of Solid State Chemistry*, 50(2):204–212, 1983.

[12] Junxin Wang, Tian Ming, Zhao Jin, Jianfang Wang, Ling-Dong Sun, and Chun-Hua Yan. Photon energy upconversion through thermal radiation with the power efficiency reaching 16%. *Nature communications*, 5(1):1–9, 2014.

[13] Hong Wang, Xiumei Yin, Mingming Xing, Yao Fu, Ying Tian, Xin , Tao Jiang, and Xixian Luo. Investigation on the thermal effects of nayf 4: Er under 1550 nm irradiation. *Physical Chemistry Chemical Physics*, 19(12):8465–8470, 2017.

[14] Blanca del Rosal, Alberto Pérez-Delgado, Elisa Carrasco, Dragana J Jovanović, Miroslav D Dramićanin, Goran Dražić, Ángeles Juarranz de la Fuente, Francisco Sanz-Rodriguez, and Daniel Jaque. Neodymium-based stoichiometric ultrasmall nanoparticles for multifunctional deep-tissue photothermal therapy. *Advanced Optical Materials*, 4(5):782–789, 2016.

[15] Wei Ren, Gungun Lin, Christian Clarke, Jiajia Zhou, and Dayong Jin. Optical nanomaterials and enabling technologies for high-security-level anticounterfeiting. *Advanced Materials*, 32(18):1901430, 2020.

Chapter 5

Conclusions

Two different security system strategies were designed, fabricated, and tested for use in printed media based on the PTT effect of Ln^{3+}-contaminated ceramic oxides. For this purpose, matrices previously reported in the literature, but which had never been reported as PTT, let alone used in security applications, were used.

Comparing the Sr/Zr hybrid ceramics samples, it was determined that a low thermal conductivity is crucial to improve the PTT response generated by the absorption of the dopant (3 W/mK for $SrZrO_3$). Excellent PTT response was verified upon excitation with a 975 nm LD at different powers, which was much more efficient than in matrices such as $NaYF_4 : 25Er^{3+}$ or $LaF_3 : Nd^{3+}$. That effectiveness correlated to the low quantum efficiency of the samples, determined through a rate equation model. Since few works explore the use of the PTT effect in security systems, this was used to design one in combination with a commercial thermochromatic pigment. This has several advantages and novelties, including ease of printing, since screen printing is used; high reliability and security, since a LD is required strictly at the absorption wavelength of the material; and the practicality of the equipment needed for decoding. These characteristics show the potential to be used in real

printed applications to verify the legal provenance of products.

Based on the conclusion of the first approach, $LaBO_3 : Nd^{3+}$ and $LaBO_3 : Yb^{3+}$ PTT particles were synthesized, which have a low thermal conductivity inherent to their orthorhombic crystalline structure (less than 6 W/mK) and a poor emission intensity. Using NIR LD, 808 nm for $LaBO_3 : Nd^{3+}$ and 975 nm for $LaBO_3 : Yb^{3+}$, the performance of the PTT effect was evaluated and found to be more effective than that of the Sr/Zr hybrid oxide samples. In addition, the fabrication cost is much lower because the precursors are cheaper, the synthesis is much simpler and shorter, and the required temperature is up to 30 % lower. For each of the samples, the thermal effect is selective and only generated with the wavelength corresponding to its absorption, which was used to design a security strategy based on multilayer codes that were revealed utilizing a thermal camera. Various security strategies were demonstrated, using individual inks or combining them to generate complex codes that were revealed through a sequence. To increase the range of options as well as the level of security, commercial particles with upconversion emission were used so that the visible channel was also included in the development sequences. Due to the advantages of the printing system (screen printing), the high security produced by the combination of excitation sources, and the development sequence in the thermal and visible image, the proposed strategy presents the feasibility and potential to be used in printed anti-counterfeiting media. Proof of this is the conceptual examples made on medicine packaging, banknotes, and business cards.

The use of wavelengths in NIR in the designed approaches complicates the reproduction of the system as it is not a visible wavelength. In addition to improving the printed system, since it avoids the generation of spurious radiation such as that produced by UV sources on paper or textiles.

In the literature, the PTT response in the matrices synthesized in the present

thesis has not been shown, in addition to the fact that it is higher than those reported for materials such as $NaYF_4 : 25Er^{3+}$ or $LaF_3 : Nd^{3+}$. Being a novel feature reported for this type of materials, the applications of these materials are not restricted to security but can be used in other applications such as PTT therapy or energy applications.

Future work

Due to the novelty and potential of the samples, work can continue in the following directions:

1. Deepening the origin of the PTT effect.
2. Reduction to nanometer size and evaluation of their PTT performance at that scale.
3. Determination of the PTT conversion efficiency.
4. Dopant modification.
5. Evaluation for application in PTT therapy.

Appendix A

Publications and Conferences

A.1 Publications

- **Jorge Molina-González**, Gonzalo Ramírez-García, Haggeo Desirena, and Octavio Meza. *Anti-counterfeiting strategy based on multiwavelength photothermal particles to disclose thermal imaging.* ***Accepted***, *Ceramics International.*
  Abstract: Product counterfeiting is a major problem worldwide, not only because of the economic losses but also because of the negative impact it has on society. Therefore, it becomes a constant need to propose advanced anti-counterfeiting methods or technologies which, ideally, should be non-cloneable, easy to implement, difficult to remove-reuse, and versatile. Although numerous systems already exist on the market or in the literature, some of them lack of the above specifications, which complicates their actual implementation. In this contribution, an easy-to-print, safe and non-restrictive anti-counterfeiting system based on the generation of thermal images by the photothermal effect of $LaBO_3 : Ln^{3+}$ particles is proposed. Wavelength excitation, 808 or 975 nm, for photothermal effect can be tuned by selecting properly the lanthanide ion (Nd

or Yb). The temperature generated by the synthesized samples covers a range from 25 to 300 °C approximately, when excited with the appropriate infrared laser diode (LD) at powers from 0.015 to 2.1 W. Using a simple screen-printing method, codes were printed using the$LaBO_3 : Nd^{3+}$ and $LaBO_3 : Yb^{3+}$ particles, which allow the generation of simple or complex thermal images under appropriate infrared laser radiation. The combination of the two synthesized materials allows the generation of codes whose decoding is subject to a specific sequence dependent on the excitation wavelengths. As a proof of concept, the generated codes are printed on various drug packaging, as well as on banknotes and business cards. Printing versatility and the security level generated by the sequence of multiple excitation wavelengths of thermal and visible codes allow the proposed system to be used in printed security applications.

- **Jorge Molina-González**, Abril Arellano-Morales, Octavio Meza, Gonzalo Ramírez-García, Haggeo Desirena.*An anti-counterfeiting strategy based on thermochromic pigment activated by highly Yb^{3+} doped photothermal particles.* Journal of Alloys and Compounds 850, 156709 (2021).

  Abstract: The counterfeiting of products is one of the main crimes combated by private companies and governments worldwide. Therefore, numerous anti-counterfeiting mechanisms must be designed, and the photothermal properties of rare-earth doped materials provide the opportunity to formulate increasingly complex strategies. This work presents a series of highly Yb^{3+} doped Sr/Zr hybrid oxide particles with distinctive photo-responsive features that allow the design of an innovative anti-counterfeiting system in combination with a thermochromic pigment implemented by screen printing technique. Upon

exposure of the samples to 975 nm laser diode (LD) irradiation, a fast increase of the temperature was observed, reaching temperatures from 82 to 215 °C according to the excitation power, and thus revealing the encrypted code during some seconds in a reversible way. This unique photothermal response was attributed mainly to the high amount of doping, and the inherent low thermal conductivity of the developed matrices. The reliability of the proposed system was systematically tested under different excitation wavelengths and powers, and upon exposition to an extrinsic source of heat. Such evaluation demonstrated the high-security level of the system, whose decoding can be performed only with specific light in a narrow region of the near-infrared (NIR) spectrum, additionally avoiding the use of more sophisticated equipment. The great advantages, both in manufacturing and decoding, allow our system to be implemented in anti-counterfeiting printing methods. In addition, we propose two models, the first to describe the origin of the high-temperature increase in our samples and the second to describe the dynamic temperature behavior.

- Rodolfo Peña-Rodríguez, **Jorge A. Molina-González**, Haggeo Desirena-Enrriquez, Erika Armenta-Jaime, José María Rivera, Silvia E. Castillo-Blum. *Doping of Zn-MOF with Eu^{3+} and Tb^{3+} for application in the manufacture of WLED.* Journal of Materials Chemistry C (2021).

  Abstract: A new blue light-emitting molecular–organic framework namely FQUNAM-MOF (1) was synthesized in a simple way using formic acid and zinc nitrate as precursors. In the present work, the potential of 1 as an efficient antenna for terbium and europium 3+ ions was evaluated at different dopant ratios. The compounds labelled $Eu^{3+}_{0.3-n}Tb^{3+}_{n}$@ **1** where n = 0.15, 0.18,

and 0.21, are isostructural and their luminescence properties were studied in detail. Excellent energy transfer occurs from the MOF-excited energy levels towards the $^5D_4$ state in Tb^{3+}, unlike Eu^{3+} where the sensibilization predominantly arises from the $^5D_4$ terbium state. These compounds exhibit a high solid-state quantum yield (QY) from 23.4 to 48.5%, higher than the reported values, and they show thermal stability at high temperatures. Additionally, a white light-emitting device (WLED) was prepared using a resin in which 20% (w/w) of the $Eu_{0.09}Tb_{0.21}$@**1** compound (48.5% QY) was added. It displayed a white-cold light emission colour according to the Commission Internationale de I'E´clairage (CIE) classification (applying current values of 10, 30, and 100 mA). These materials contribute to the emerging field of molecular–organic frameworks for the development of new efficient and stable lighting sources.

- A. Benítez-Lara, H. Cisneros, E. Bautista, **J. Molina**, F. Morales, E. Morales-Narváez, J. Carrillo-López, H. Desirena and O. Lopez. *Implementation of an inexpensive cathodoluminescence and electron beam induced current image generator coupled to a scanning electron microscope*. Journal of Instrumentation 16, P04005 (2021).

  Abstract: In this work, implementation of a novelty cathodoluminescence and electron beam induced current image generator system for do in situ experiments in a scanning electron microscopy (SEM) is presented. The equipment is composed by one mechatronic system (MS) with interchangeable probes and digitalization system programed with Labview. Porous silicon and $Eu_2(WO_4)_3$ microparticles were characterized in cathodoluminescense mode with luminescence peaks centered at 410 and 613 nm, respectively. For CL imaging, the

emission signal is collected through a probe of nine optical fibers and transduced to an electrical signal via a photomultiplier tube (PMT). In other way, the configuration in EBIC mode was tested with commercial silicon monocrystalline solar cell to determine internal defects using a current mapping. However for EBIC imaging, the current is collected by two electrodes connected to a picoammeter synchronized with the electron beam. CL and EBIC images are compared with SE images and chemical elemental mapping images to correlate the emission and defects regions of the sample.

- A.Arellano-Morales, **J.Molina-González**, H.Desirena, J.M.Bujdud-Perez, S.Calixto. *High CRI in phosphor-in-doped glass under near-ultraviolet excitation for warm white light-emitting diode.* Journal of Luminescence 229, 117684 (2021).
  Abstract:A series of phosphor-in-doped glass (PiDG) were fabricated through a CO_2 laser heating, blending commercial green phosphor $SrAl_2O_4 : Eu^{2+}$ and Eu^{3+}-doped boro-tellurite glass powders. Translucent PiDGs with low loss of the emissive properties of the $SrAl_2O_4 : Eu^{2+}$ phosphor can be only achieved through CO_2 laser heating; whereas, sintering of PiDGs by means of the conventional method (electric furnace) lead to opaque samples with loss of entire of green emission. Long exposure time of the CO_2 laser modifies the PiDGs melt volume due to temperature rise, increasing their diameter and thickness. The fast cooling of CO_2 laser approach allows the sintering of transparent PiDGs, avoiding opaque samples and low radiometric properties. A warm white light-emitting diode (w-LED) prototype was fabricated by placing PiDGs on top of a near-ultraviolet (n-UV) chip at 385 nm, showing a high color rendering index (CRI) and a low correlated color temperature (CCT) of 88 and 2369 K

respectively. However, a lower CCT with a detriment of CRI can be achieved by using a low $SrAl_2O_4 : Eu^{2+}$ phosphor concentration. The PiDGs obtained show enormous potential to be applied as a phosphor converter in warm w-LEDs for residential applications.

- A Arellano-Morales, **J Molina-González**, H Desirena, J Hernandez, Sergio Calixto. *Fast sintering method of phosphor-in-glass for high-power LEDs.* Journal of Luminescence 214, 116546 (2019).

  Abstract: Fast sintering of Phosphor-in-Glass (PiG) by means of CO_2 laser heating has been successfully achieved. PiGs samples fabricated at different exposure times were characterized and compared with a PiG sample synthetized through an electric furnace. An exposure time as short as 30 s and 12 W of optical power is necessary to sintering PiGs. Results show that the optimization of CO_2 laser approach can dramatically reduce up to 60 times the PiGs sintering. Luminous Efficacy (LE) of at least 79.7 lm/W as well as minimum Color Rendering Index (CRI) value of 70 for all fabricated PiGs were obtained. Correlated Color Temperature (CCT) value decreased gradually as the CO_2 laser exposure time increased. These results show that PiGs samples, synthetized with short exposure times, show excellent lighting properties.

- Rodolfo Peña-Rodríguez, **Jorge A. Molina-González**, Haggeo Desirena-Enrriquez, José Ma Rivera-Villanueva, Silvia E. Castillo-Blum. *Tunable luminescence modulation and warm light emission of Zn-MOF (4,4-bipyridyl and zinc acetate) doped with Eu3+ and Tb3+.* Materials Chemistry and Physics 223, 494-502 (2018).

Abstract: Herein, we describe the synthesis and doping of Zn-MOF (4,4-bipyridyl and zinc acetate), crystallographic structure, optical properties of heteronuclear coordination polymers with emission in the visible (Eu^{3+}/Tb^{3+} and Zn-MOF). The MOF presents a linear structure in the form of a nanotube. Density functional theory (DFT) and time dependent-DFT calculations were performed on the ground and excited states of Zn-MOF to provide insight of geometries, frontier molecular orbitals, and singlet and triplet state energies of the polymer. The metal-organic framework was doped with Eu^{3+} or Tb^{3+} in different proportions ($Eu_{0.5-n}Tb_n@Zn-MOF$, when n=0.00, 0.05, 0.10, 0.15, ..., 0.5). The doped Zn-MOFs exhibit the typical red and green emission corresponding to Eu^{3+} and Tb^{3+} ions, respectively, energy transfer from MOF to metal ions takes place ("antenna effect"). It is noteworthy that the emission color of the lanthanides doped Zn-MOFs changes from red to orange-yellow-green depending on the proportion between Eu^{3+} and Tb^{3+}. These compounds presented a τ ranging from 1.29 to 1.62 and 1.06 - 1.56 ms for Eu^{3+} and Tb^{3+}, respectively, and the corresponding absolute quantum yields values range from 38 to 61%.

- Haggeo Desirena, **Jorge Molina-González**, Octavio Meza, Priscilla Castillo, Juan Bujdud-Pérez. *Multicolor and Warm White Emissions with a High Color Rendering Index in a Tb^{3+}/Eu^{3+}-Codoped Phosphor Ceramic Plate.* Materials 12, 2240 (2019).

  Abstract: A series of Tb^{3+}/Eu^{3+}-codoped phosphor ceramic plates with a high color rendering index (CRI) for a near-ultraviolet light emitting diode (LED) were fabricated. Color emission can be tuned from green to reddish

as a function of Eu^{3+} concentration. By doping only 0.15 mol% of Eu^{3+} concentration, a comfortable warm white emission is promoted as a result of simultaneous emissions of Tb^{3+} and Eu^{3+} ions. A theoretical model is proposed to calculate the contributions of the emitted color of the donor (Tb^{3+}) and acceptor (Eu^{3+}) ions in terms of europium concentration. The energy transfer from Tb^{3+} to Eu^{3+} ions is corroborated by the luminescence spectra and decay time of Tb^{3+}, with a maximum energy transfer efficiency of 76% for 28 mol% of Tb^{3+} and 14 mol% of Eu^{3+}. Warm white LEDs were constructed using a 380 nm UV chip and showed a CRI of 82.5, which was one of highest values reported for Tb^{3+}/Eu^{3+}-codoped samples. Color-correlated temperature (CCT), color coordinate (CC), and luminous efficacy (LE) were utilized to know the potentials as a phosphor converter in solid-state lighting.

- I.E. Orozco Hinostroza, H. Desirena, J. Hernadez, **J. Molina**, I. Moreno, and E. De la Rosa. *Eu3+ - doped glass as a color rendering index enhancer in phosphor-in-glass*. Journal of the American Ceramic Society 101, 2914–2920 (2018).

  Abstract:A new method for improving color rendering index (CRI) and low correlated color temperature (CCT) in high-power white-light-emitting diodes (WLEDs) is proposed. We used a configuration of phosphor-in-glass (PIG) and studied light output changes with the increment in concentration of yellow-emitting $Y_3Al_5O_{12} : Ce^{3+}$(YAG:Ce3+) phosphor. The PIG was coupled on the top of blue-light-emitting diodes (LED) chip (465 nm). To compensate the lack of red emission in the phosphor, Eu^{3+}-doped tellurium glass with different europium content was employed as a red emitter. The suitable contents of

YAG:Ce^{3+} and Eu^{3+} were 7.5 weight percent (wt%) and 3 mol percent (mol%), respectively. The CRI value went from 72 to 82, whereas the CCT was reduced from 24 933 to 6434 K. The proposed structure can improve CCT as well as CRI of WLEDs just by placing a glass on top.

A.2 Conference presentations

- *Printed anti-counterfeiting strategies based on the photothermal effect of lanthanide-doped ceramic particles.* MOPM (November 2021).
- *A novel anti-counterfeiting approach: thermochromic pigment activated by* Yb^{3+} *doped photothermal particles.* SPIE Photonic West (March 2021).
- Tb^{3+}/Eu^{3+} *Ceramic phosphor plate as potential material for solid state lighting.* RIAO-OPTILAS-MOPM (September 2019).
- *Intense red emission* Eu^{3+} *doped glass-ceramics: New materials for lighting applications.* Congreso Nacional de Física (July 2020).